JℲM PAPERS

Airfoil synchronous surging and pitching

C. Strangfeld[1,3] , H.F. Müller-Vahl[2], C.N. Nayeri[3], C.O. Paschereit[3] and D. Greenblatt[2]

[1]Department 8 Non-Destructive Testing, Bundesanstalt für Materialforschung und - prüfung, Unter den Eichen 87, Berlin 12005, Germany
[2]Faculty of Mechanical Engineering, Technion - Israel Institute of Technology, Haifa 3200003, Israel
[3]Hermann-Föttinger Institut, Institute of Fluid Dynamics and Technical Acoustics, Technische Universität Berlin, Müller-Breslau-Str 8, Berlin 10623, Germany
Corresponding author: David Greenblatt, davidg@technion.ac.il

Combined surging and pitching of an airfoil at the identical frequency (i.e. synchronously), at four different phase differences, was investigated theoretically and experimentally. The most general unsteady theoretical formulation was adopted to calculate the lift coefficient, and then extended to explicitly compute the unsteady bound vortex sheet. This was used for comparison with experiments and facilitated the computation of both Joukowsky and impulsive-pressure lift contributions. Experiments were performed using a symmetric 18 % thick airfoil in an unsteady wind tunnel at an average Reynolds number of 3.0×10^5, with a free-stream oscillation amplitude of 51 %, an angle-of-attack range of $2° \pm 2°$ and a reduced frequency of 0.097. In general, excellent correspondence was observed between theory and experiment, representing the first direct experimental validation of the general theory. It was shown, both theoretically and experimentally, that the lift coefficient was not accurately represented by independent superposition of surging and pitching effects, due to variations in the instantaneous effective reduced frequency not accounted for during pure pitching. Deviations from theory, observed at angle-of-attack phase leads of 90° and 180°, were attributed to bursting of separation bubbles during the early stages of the acceleration phase. The largest deviations occurred when the impulsive-pressure lift contribution was small relative to the Joukowsky contribution, because the latter was most affected by bubble bursting. Bubble bursting resulted in large form-drag oscillations that occurred at identical phase angles within the oscillation cycle, irrespective of the phase difference between surging and pitching, as well as in the absence of pitching.

Key words: unsteady aerodynamics, dynamic stall, separation bubble, bubble bursting

C. Strangfeld, H.F. Müller-Vahl, C.N. Nayeri, C.O. Paschereit and D. Greenblatt

1. Introduction

Low-speed unsteady aerodynamics is concerned with determining the unsteady loads on fixed wing aircraft (e.g. Bisplinghoff, Ashley & Halfman 2013; Jones, Cetiner & Smith 2022), rotorcraft (e.g. Sharma & Visbal 2019; Gardner *et al.* 2023), drones (e.g. Oo *et al.* 2023), wind turbines (e.g. Ferreira *et al.* 2009; Simms *et al.* 2001; Buchner *et al.* 2018) and flapping-wing flyers (e.g. Taylor *et al.* 2003). The majority of idealised studies involve two-dimensional airfoils undergoing dynamic rotation or translation, most commonly by periodic pitching or plunging (see references in the reviews by Corke & Thomas 2015; Bergami, Gaunaa & Heinz 2013; Turhan, Wang & Gursul 2022). During the last decade, streamwise (or longitudinal) oscillation of the flow or test article– often called surging– has received increased attention (e.g. Granlund *et al.* 2014; Choi, Colonius & Williams 2015; Dunne & McKeon 2015; Medina *et al.* 2018; Müller-Vahl *et al.* 2020) due to its relevance to rotorcraft and wind turbines. Surging studies present the technical challenge of attaining large relative amplitudes ($\sigma \equiv \Delta u/u_s \gtrsim 20\%$), where Δu is the oscillating velocity amplitude, at practically relevant reduced frequencies $k \equiv \omega c/2u_s$ and several different approaches have been proposed (e.g. Greenblatt, Kiedaisch & Nagib 2001; Granlund *et al.* 2014; Gloutak, Jansen & Farnsworth 2024). Here u_s is the cycle-averaged free-stream velocity, ω is the circular frequency and c is the chord length. In contrast to pitching and plunging, surging can introduce significant time-dependent Reynolds number effects (e.g. Carmichael 1981; Toppings & Yarusevych 2023), typically observed when $Re(t) \equiv u(t)c/\nu \lesssim 10^5$, where $u(t)$ is the time dependent free-stream velocity and ν is the kinematic viscosity.

Recently, investigators have recognised the importance of studying surging at nominally pre-stall angles-of-attack (Strangfeld *et al.* 2016; Yang *et al.* 2017; Zhu *et al.* 2020; Duncan, Cai & Gunasekaran 2024; Gloutak *et al.* 2024; Wang *et al.* 2024). Two of these studies considered relatively high $\{Re_s, \sigma\}$ NACA 0018 experiments (Strangfeld *et al.* 2016; Zhu *et al.* 2020,the first one being our own) in the range $0° \leqslant \alpha \leqslant 4°$. With an aerodynamically smooth low-pressure airfoil surface, the phase-averaged lift coefficient $C_l(\phi)$ in our investigation showed an anti-correlation with the theories of Greenberg (1947) and Isaacs (1945). However, with the boundary layer passively perturbed by a two-dimensional discontinuity (slot) at $x/c = 5\%$, the lift coefficient corresponded with theory, but high-frequency oscillations were observed during the early stages of the acceleration phase. In a follow-up study (Greenblatt, Müller-Vahl & Strangfeld 2023), we presented compelling evidence that the high-frequency oscillations are due to bursting of the laminar separation bubbles (LSBs) on both surfaces of the airfoil. We further hypothesised that the tripping effect of the slot perturbation on the LSB acts to delay or prevent its bursting (Marxen & Henningson 2011; Yarusevych & Kotsonis 2017) and, therefore, this was the most likely reason for the improved correspondence with theory. The suspected bubble bursting also manifested as large differences between corresponding unsteady and quasi-steady form-drag coefficients $C_d(\phi)$ and $C_{d,qs}(\phi)$. Phase-averaged lift coefficient $C_l(\phi)$ data of Zhu *et al.* (2020) showed significant deviations from the theory of Isaacs (1945). In particular, under the conditions $\sigma = 0.23$ and $k = 0.05$, the measured lift coefficient exceeded the theoretical value by an order of magnitude with multiple local lift peaks. Using a technique known as background-oriented Schlieren visualisation, they demonstrated that the classical Kutta condition is violated under surging. This was attributed to either a pressure difference across trailing edge due to viscosity (based on the analysis of Taha & Rezaei 2019), or trailing-edge separation. The trailing-edge separation hypothesis advanced by Zhu *et al.* (2020) is consistent with our own observations of bubble bursting.

The combined effect of simultaneous surging and pitching on airfoil loads is a scenario that has greater direct practical relevance, particularly as an idealised representation of

1009 A41-2

helicopter and wind turbine aerodynamics. The majority of these studies (e.g. Granlund *et al.* 2014; Choi *et al.* 2015; Dunne & McKeon 2015), including our own (Medina *et al.* 2018; Müller-Vahl *et al.* 2017,2020), focus on the phenomenon of dynamic stall observed at post-stall angles-of-attack $\alpha > \alpha_s$, due to its technological importance. One exception is the experimental NACA 0015 airfoil study of Ma *et al.* (2021), where small pitch amplitude oscillations of $\Delta\alpha = 1°$ and $2°$ around zero in the presence of surging with $\sigma = 0.2$ were considered. The pitching and surging frequencies were different, with no phase relationship between them, and the data showed similar trends to the theory of Greenberg (1947). In contrast to the study of Ma *et al.* (2021), idealised rotorcraft and wind turbine blades experience simultaneous, or synchronous, surging and pitching, i.e. the frequency of both is the same although they are generally not in phase. In particular, on high-speed (co-axial, rigid rotor) helicopters that fly at high advance ratios $\mu \equiv V/\Omega R$, where V is the flight speed, Ω is the rotor speed and R is the rotor radius, the highly loaded outboard parts of the blades are subjected to high-amplitude surging with synchronous pre-stall angle-of-attack oscillations (Barbely & Komerath 2016; Feil, Hajek & Rauleder 2020; Singh & Friedmann 2021). To the best knowledge of the authors, no synchronous high-amplitude surging and pre-stall pitching experiments have been performed. Therefore, one objective of the present research is to perform and analyse such experiments.

In order to analyse the results of the proposed experiments, comparisons with theory must be conducted. On the one hand, the theory of Theodorsen (1935) is used to predict the unsteady lift and pitching moments due to various harmonic airfoil motions like pitching, plunging or flap deflections with a constant free stream. On the other hand, the theory of Isaacs (1945) computes the unsteady lift and pitching moments of an airfoil at a constant angle-of-attack subjected to a harmonically varying free stream. The theory of Greenberg (1947) considers the same problem but due to the so-called high-frequency assumption, this theory is limited to relatively small velocity ratios σ below 0.4 (van der Wall & Leishman 1994; Strangfeld *et al.* 2014). However, Isaacs extended his theory to incorporate both degrees of freedom, i.e. surging and mid-chord pitching simultaneously (Isaacs 1946). Based on this more general analysis, van der Wall (1991) further extended the theory to include an arbitrary pitch axis, the consideration of arbitrary harmonic pitch profiles and arbitrary vertical airfoil motion.

Although the formulation of van der Wall (1991) is the most general, only integral expressions containing the bound vortex sheet strength γ_b were derived. So, while the formulation is sufficient to derive the unsteady lift and moments, it does not provide explicit variation of γ_b along the chord. As a consequence, comparisons with locally measured vortex sheet strengths– based on the measurement of corresponding chordwise pressure differences across the airfoil's suction and pressure surfaces– are not possible. Furthermore, calculation of the total lift in van der Wall (1991) is based on the separation of lift into the so-called 'Joukowsky' and 'impulsive-pressure' lift components. However, in order to obtain these, complex integral transformations require rearrangement of the components as circulatory and non-circulatory, likely followed by inverse integral transformations of the unsteady lift into Joukowsky and impulsive-pressure components. These inverse transformations do not appear to have ever been performed. To bypass this, we develop an explicit relation for γ_b, which we solve by employing the integral solutions presented in our previous research (see the Appendix in Strangfeld *et al.* 2016). Although this approach results in longer computation times – because hyperbolic Bessel functions and confluent hypergeometric Kummer functions are part of the solution – the Joukowsky and impulsive-pressure components can be computed directly. We will show in this paper that the quantification of these separate lift components is very valuable for the interpretation of experimental data.

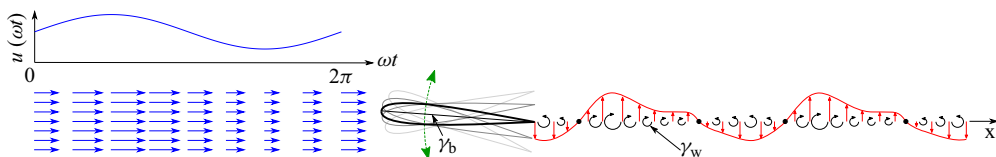*C. Strangfeld, H.F. Müller-Vahl, C.N. Nayeri, C.O. Paschereit and D. Greenblatt*

Figure 1. Schematic illustrating a pitching airfoil in a surging free stream, which generates an unsteady wake vortex sheet.

In summary, almost all experimental studies involving synchronous surging and pitching focus on the problem of dynamic stall, where the static stall angle is exceeded. Furthermore, all of these studies are confined to Reynolds numbers less than 10^5. The only exception involves small pitch amplitude oscillations of $\Delta\alpha = 1°$ and $2°$, without any phase relationship enforced between surging and pitching. In terms of theory, circulatory and non-circulatory lift coefficients can be calculated, but this tells us nothing about the vortex sheet strength distribution and, as a consequence, no information can be gleaned about the Joukowsky lift and the impulsive-pressure lift. The objective of the present research, therefore, is to study, both theoretically and experimentally, the effects of synchronous surging and pitching on an airfoil at low pre-stall angles-of-attack ($0° \leqslant \alpha \leqslant 4°$). The theoretical approach follows the methods developed by van der Wall & Leishman (1994) for synchronous surging and pitching, and then extends them to calculate the bound, unsteady, vortex sheet strength distributions, as well as the Joukowsky and impulsive-pressure lift components. These theoretical developments are presented in § 2. The experiments were performed on the previously used NACA 0018 in the Technion's unsteady wind experimental set-up, which is described in § 3. We extended the tripped low-surface-pressure cases that corresponded with theory under pure surging (i.e. surging at constant α), by adding synchronous pitching at four different phase differences, namely $\tau = 0°$, $90°$, $180°$ and $270°$. These experiments were designed specifically to obtain high-precision quasi-steady and unsteady phase-averaged pressure coefficient measurements. The main results of both the experimental and theoretical components of this investigation are presented in § 4. Much like our pure surging study, comparisons of the measured and theoretical vortex sheet strengths are used to determine the limits of the theory and, in particular, the impact of separation bubble bursting. Furthermore, we directly compare unsteady surface-pressure coefficients with their quasi-steady counterparts in order to understand the bubble-bursting mechanism and its effect on the form-drag coefficient.

2. Surging and pitching airfoil theory

2.1. *Unsteady lift overshoot in potential flow*

The problem considered in this paper is illustrated schematically in figure 1, that shows an airfoil (in our case, a NACA 0018 airfoil) that is pitched harmonically about its quarter-chord position (green arrow), while the free stream surges harmonically at the identical frequency. The length of the blue arrows schematically illustrates the time-varying velocity amplitude, and the phase difference between the free stream and angle-of-attack is assigned the symbol τ. The lift force acting on the airfoil at any phase angle ϕ, which is proportional to the circulation of the bound vortex sheet, is affected by a combination of the unsteady inflow and airfoil motion. According to Helmholtz's circulation theorem, the overall circulation in the global system must remain constant. Thus, a circulation change of arbitrary strength at one time step requires the simultaneous shedding of a vortex into the wake with opposite strength (illustrated by the black wake vortices and red line).

The shed wake vorticity induces normal velocities on the airfoil which modify the circulation change and hence the generated lift. The higher the velocity amplitudes σ or the reduced frequencies k, the larger the influence of the wake vorticity.

2.2. *Theoretical approach of van der Wall*

Theories for unsteady airfoil lift and pitching moments, first introduced by Theodorsen (1935), invoke the assumption that the airfoil is modelled as a two-dimensional (infinite-span) flat plate in an incompressible potential flow. The boundary layer is modelled as a vortex sheet, approximating a thin airfoil at high Reynolds number under fully attached flow, and hence no explicit friction forces, diffusion or separation exist. Throughout the derivation of the closed form solution presented here, only small angles-of-attack are considered. In the case of an unsteady, sinusoidal free stream, the maximum amplitude of the velocity oscillation is limited to $\sigma \leqslant 1$ to prohibit reverse flow.

Consider an airfoil submerged in an incompressible free-stream velocity, that is surging according to

$$u(\phi) = u_s(1 + \sigma \sin(\phi)), \tag{2.1}$$

and whose angle-of-attack is oscillating according to

$$\alpha(\phi) = \alpha_0 \left[\bar{\alpha}_0 + \sum_{n=1}^{\infty} [\bar{\alpha}_{nS} \sin(n\phi) + \bar{\alpha}_{nC} \cos(n\phi)] \right], \tag{2.2}$$

where α_0 is the cycle-averaged angle-of-attack, the $\bar{\alpha}$ terms are dimensionless amplitude coefficients and $\phi = \omega t$. The frequencies of the free-stream and pitch oscillations ω are identical, hence only one global k, based on the average free-stream velocity u_s, is used. According to van der Wall (1991), the unsteady-to-quasi-steady lift coefficient ratio as a function of ϕ is

$$\begin{aligned}
\frac{C_l(\phi)}{C_{l,qs}} &= \frac{1}{(1 + \sigma \sin(\phi))^2} 0.5k[(\sigma\bar{\alpha}_0 + \bar{\alpha}_{1S} + k(a\bar{\alpha}_{1C}) - 0.5\sigma\bar{\alpha}_{2C}) \cos(\phi) \\
&\quad + (-\bar{\alpha}_{1C} + k(a\bar{\alpha}_{1S} - 0.5\sigma\bar{\alpha}_{2S}) \sin(\phi) \\
&\quad + \sum_{n=2}^{\infty} n(\bar{\alpha}_{nS} + nka\bar{\alpha}_{nC} + 0.5\sigma(\bar{\alpha}_{(n-1)C} - \bar{\alpha}_{(n+1)C})) \cos(n\phi) \\
&\quad + \sum_{n=2}^{\infty} n(-\bar{\alpha}_{nC} + nka\bar{\alpha}_{nS} + 0.5\sigma(\bar{\alpha}_{(n-1)S} - \bar{\alpha}_{(n+1)S})) \sin(n\phi)] \\
&\quad + \frac{1}{(1 + \sigma \sin(\phi))^2} \left[((1 + 0.5\sigma^2)\bar{\alpha}_0 + \sigma(\bar{\alpha}_{1S} - 0.5k((0.5 - a)\bar{\alpha}_{1C}) \right. \\
&\quad \left. - 0.25\sigma\bar{\alpha}_{2C})) \cdot (1 + \sigma \sin(\phi)) + \sum_{m=1}^{\infty} (\Re(l_m) \cos(m\phi) + \Im(l_m) \sin(m\phi)) \right], \tag{2.3}
\end{aligned}$$

where the normalised distance of the quarter-chord pitch axis to the midchord corresponds to $a = -0.5$. The first four lines in (2.3) express the non-circulatory part of the unsteady lift effects and the last two lines express the circulatory part that include a summation from the first wavenumber $m = 1$ to infinity. Equation (2.3) furthermore requires the real $\Re$ and imaginary $\Im$ parts of l_m, where

$$l_m = -2m(i)^{-m} \sum_{n=1}^{\infty} [F_n(J_{n+m}(n\sigma) - J_{n-m}(n\sigma))$$
$$+ iG_n(J_{n+m}(n\sigma) + J_{n-m}(n\sigma))], \tag{2.4}$$

$$F_n + iG_n = [C(nk)]n^{-2}(H_n(n\sigma) + iH'_n(n\sigma)). \tag{2.5}$$

The most general formulation of these coefficients is given by van der Wall (1991), which includes Bessel functions of the first kind J, the Theodorsen (1935) function $C(nk) = F(nk) + iG(nk)$ and

$$H_n(n\sigma) = \frac{J_{n+1}(n\sigma) - J_{n-1}(n\sigma)}{2}[\sigma\bar{\alpha}_0 - \bar{\alpha}_{1s} - k(0.5 - a)\bar{\alpha}_{1c}] - \frac{2J_n(n\sigma)}{n\sigma}\bar{\alpha}_{1s}, \tag{2.6}$$

$$H'_n(n\sigma) = \frac{J_{n+1}(n\sigma) - J_{n-1}(n\sigma)}{n}\bar{\alpha}_{1c} + \frac{J_n(n\sigma)}{\sigma}\left[\bar{\alpha}_{1c}(1 - \sigma^2) - k(0.5 - a)\bar{\alpha}_{1s}\right]. \tag{2.7}$$

The formulation of the coefficients H_n and H'_n in (2.6) and (2.7) implicitly assumes angle-of-attack oscillations of the form expressed in (2.2). A more general formulation for arbitrary oscillatory motions can be found in van der Wall (1991).

If a constant angle-of-attack is assumed, (2.3) reduces to the formulation of Isaacs (1945). Similarly, if the amplitude of the free-stream velocity oscillation is zero, (2.3) is equivalent to the formulation of Theodorsen (1935). This fortunately obviates the need for a separate presentation of the theories. Furthermore, (2.3) depicts the lift coefficient ratio with $C_l(\phi)/C_{l,qs} = L(\phi)/L_{qs}(1 + \sigma \sin(\phi))^{-2}$, where the quasi-steady lift $L_{qs} = \pi\rho cu_s^2\alpha$ is determined from steady thin airfoil theory (Anderson 2011). The ratio of lift coefficients, as opposed to the ratio of lift forces, is employed here because it clearly shows the net unsteady effects that can otherwise be overwhelmed by the oscillations in dynamic pressure.

Finally, in order to explicitly include the phase shift τ in the formulation, we let $\alpha_0 = \alpha_s$, $\bar{\alpha}_0 = 1$, $\alpha_{1S} = \alpha_a \cos(\tau)\alpha_s^{-1}$ and $\alpha_{1C} = \alpha_a \sin(\tau)\alpha_s^{-1}$ in (2.2), which can be written as

$$\alpha(\phi) = \alpha_s + \alpha_a[\sin(\phi)\cos(\tau) + \cos(\phi)\sin(\tau)] = \alpha_s + \alpha_a \sin(\phi + \tau). \tag{2.8}$$

2.3. *Derivation of the shed wake vorticity*

In the previous section, the phase-dependent lift coefficient ratio due to surging and pitching was presented. While this ratio is useful for identifying integral unsteady effects, it does not reveal the local circulation distribution, or vortex sheet strength, along the chord. This distribution is important for two reasons. First, it can be measured in experiments and hence used directly for validation of the theory. Second, deviations from the theory are useful for identifying effects of boundary layer separation. Thus, we seek a new expression for the unsteady bound vortex sheet $\gamma_b(x, t)$ with $x = (c/2) \cos \Theta$. The first step in this process is the calculation of the time-varying shed wake vorticity strength, which results in induced chord-normal velocities that play a crucial role in determining the unsteady lift variation. The normal velocity distribution along the chord, based on van der Wall (1991) for small α can be expressed as

$$v_{n,b}(x, t) = \alpha(t)u(t) + (x - 0.5ac)\dot{\alpha}(t) + \dot{h}(t) + v_{n,w}(x, t). \tag{2.9}$$

The first term includes both the unsteady angle-of-attack as well as the unsteady free-stream velocity, the second term enables an arbitrary positioning of the pitch axis relative to the mid-chord, the third term defines a time-varying vertical airfoil motion and the last term depicts the contribution of the shed vorticity in the wake.

The shed vorticity is generated continuously at the trailing edge and convects downstream, and therefore the shed wake vorticity strength is the time derivative of the unsteady bound circulation, designated $\dot{\Gamma}(\tau^*)$. These shed wake vortices induce velocity components normal to the chord as described by the Biot–Savart law (Schade *et al.* 2007) and thus at each instant in time τ^*, the entire unsteady wake needs to be taken into account to determine valid unsteady effects. The wake-induced normal velocities can thus be expressed by

$$v_{n,w}(\Theta, t) = -\frac{1}{2\pi} \int_{-\infty}^{t} \frac{\dot{\Gamma}(\tau^*)}{1 + \frac{W(t) - W(\tau^*)}{0.5c} - \cos(\Theta)} \mathrm{d}\tau^*, \tag{2.10}$$

where $W(t)$ is the distance travelled by the airfoil with the coordinate transformation $x = (C/2)\cos(\Theta))$ (van der Wall 1991). Normalisation by the half-chord $c/2$ and transformation into a Fourier series yields $v_{n,w}(\Theta, t) = b_0(t)/2 + \sum_{n=1}^{\infty} b_n(t)\cos(n\Theta)$. Furthermore, the self-induced normal velocities $v_{n,b}$ caused by the bound vorticity sheet γ_b are given by

$$v_{n,b}(\Theta, t) = \frac{1}{2\pi} \int_{0}^{\pi} \frac{\gamma_b(\theta, t)\sin\theta}{\cos(\Theta) - \cos(\theta)} \mathrm{d}\theta, \tag{2.11}$$

and its transformation into a Fourier series gives $v_{n,b}(\Theta, t) = d_0(t)/2 + \sum_{n=1}^{\infty} d_n(t) \cos(n\Theta)$. Now, all quantities in (2.9) are known except for the vorticity sheet γ_b which gives the circulation by integration along the chord $\Gamma(t) = \int_{-c/2}^{c/2} \gamma_b(x, t)\mathrm{d}x$. The condition of flow tangency is required to solve this problem, and thus the condition

$$v_n(x, t) \equiv 0 = \alpha(t)u(t) + (x - 0.5ac)\dot{\alpha}(t) + v_{n,w}(x, t) - v_{n,b}(x, t), \tag{2.12}$$

is enforced (see (2.9)) where vertical plunging motion is not considered. A comparison of the Fourier series coefficients yields the following identities (Isaacs 1945):

$$c_0(t) = 2\alpha(t)u(t) + c(0.5 - a)\dot{\alpha}(t) + b_1(t) + b_0(t), \tag{2.13}$$

$$c_1(t) = -2\alpha(t)u(t) + ac\dot{\alpha}(t) + b_2(t) - b_0(t), \tag{2.14}$$

$$c_2(t) = -0.5c\dot{\alpha}(t) + b_3(t) - b_1(t), \tag{2.15}$$

$$c_n(t) = b_{n+1}(t) - b_{n-1}(t) \qquad n \geqslant 3. \tag{2.16}$$

Furthermore, the Kutta condition requires finite velocities at the wing's trailing edge $c_0(t) = -\sum_{n=1}^{\infty} c_n(t)$ (Amiet 1990) and $c_0(t)$ satisfies this condition, because b_n converges to zero for $n \to \infty$. Finally, the circulation is expressed in cylindrical coordinates according to Isaacs (1945) as

$$\begin{aligned} \Gamma(t) &= \frac{c}{2} \int_{0}^{\pi} \gamma_b(\Theta, t)\sin(\Theta)\mathrm{d}\Theta \\ &= \frac{c}{2} \int_{0}^{\pi} \left[c_0(t) + \sum_{n=1}^{\infty} c_n(t)\cos(n\Theta) \right] \mathrm{d}\Theta = \frac{\pi c}{2} c_0(t). \end{aligned} \tag{2.17}$$

Equation (2.17) is a concise and elegant interim result for the time-varying circulation, where only the coefficient $c_0(t)$ is required. Furthermore, all $c_n(t)$ are functions of $b_n(t)$ which themselves vary only in time. Thus, the spatial variable x or Θ is eliminated. The formulation in (2.17) leads to an integro-differential equation for $\Gamma(t)$

$$b_n(t) = -\frac{2}{\pi c} \int_0^\infty \dot{Q}(W(t) - \Lambda) \frac{\left[1 + 2\Lambda/c - \sqrt{(1 + 2\Lambda/c)^2 - 1}\right]^n}{\sqrt{(1 + 2\Lambda/c)^2 - 1}} \, d\Lambda, \qquad (2.18)$$

with $\Lambda = W(t) - W(\tau^*)$ and $\dot{Q}(W(t) - \Lambda) = \dot{\Gamma}(t - T) = \dot{\Gamma}(\tau^*)$. Under the assumption that all explicit variables, for example $u_s(t)$ and $\alpha(t)$, are periodic in time with the angular frequency $\omega = 2\pi f$ and the transient starting process is ignored, the resulting circulation $\Gamma(t)$ is periodic in time as well. Thus, the time derivation of the circulation, which is equivalent to the shed wake vorticity strength, is expressed as

$$\dot{Q}(W(t) - \Lambda) = \sum_{m=-\infty}^\infty a_m i m \frac{\omega}{u_s} e^{im\omega(W(t) - \Lambda)/u_s}. \qquad (2.19)$$

Since $W(t)$ describes the distance travelled by the airfoil through the unsteady inflow, it is the time integral of the free-steam velocity $u_s(t)$. The most general formulation of the coefficients a_m is given by van der Wall (1991) (the coefficient $imkc/2$ in equation B.41 in van der Wall (1991) contains a typographical error, the coefficient in front of the integral must be $imk2/c$; this typographical error has no consequence for the rest of van der Wall (1991)), where

$$a_m = \frac{A_m}{R_m}, \qquad (2.20)$$

$$R_0 = 1, \qquad (2.21)$$

$$R_m = 1 + imk\frac{2}{c} \int_0^\infty e^{-im\frac{\omega\Lambda}{u_s}} \left(\sqrt{\frac{c}{\Lambda} + 1} - 1\right) d\Lambda, \qquad (2.22)$$

$$A_0 = \pi c \alpha_s u_s \left[\left(1 + \frac{\sigma^2}{2}\right) \bar{\alpha}_0 + \sigma \left(\bar{\alpha}_{1s} - \frac{k}{4}(1 - 2a)\bar{\alpha}_{1c}\right)\right], \qquad (2.23)$$

$$A_m = \frac{i^m}{m} \pi c \alpha_s u_s (H_m(m\sigma) + i H_m'(m\sigma)). \qquad (2.24)$$

Oscillating free-stream and unsteady pitching motions are included in the above coefficients, which represent a closed-form solution of the unsteady wake. By means of the known shed vorticity, the circulation of the airfoil can now be determined from (2.17). Thus only the two coefficients $c_0(t)$ and $c_1(t)$ need to be evaluated for the desired unsteady motion as described in Isaacs (1946) and van der Wall (1991).

The integral formulation of the unsteady lift bypasses the calculation of $c_n = b_{n+1} - b_{n-1}$ with $n \geqslant 2$, although these coefficients are non-zero. This approach reduces the computational effort significantly, but introduces two disadvantages. Firstly, the bound vortex sheet distribution along the chord cannot be calculated and, secondly, the Joukowsky lift and the impulsive-pressure lift cannot be obtained. The rearrangement of the transformed integrals results in the formulation of circulatory and non-circulatory lift. This expression deviates from the initially formulated Joukowsky and impulsive-pressure lift, although the sum of the two corresponding lift contributions is always identical.

2.4. *Calculation of the unsteady bound vortex sheet*

The starting point for the new derivation of the unsteady bound vortex sheet is

$$\gamma_b(\Theta, t) = \frac{c_0(t) + \sum_{n=1}^\infty c_n(t) \cos(n\Theta)}{\sin(\Theta)}, \qquad (2.25)$$

where all of the coefficients c_n are required (Strangfeld 2015). Although the limits of the unsteady bound vortex sheet are consistent with the steady case (Strangfeld *et al.* 2014), the time-varying coefficients c_n are still unknown in (2.25). Equation (2.18), combined with the periodic formulation of the unsteady shed vorticity in (2.19), leads to

$$b_n(t) = -\frac{2}{\pi c} \int_0^\infty \sum_{m=-\infty}^\infty a_m im \frac{\omega}{u_s} e^{im\omega(W(t)-\Lambda)/u_s}$$
$$\cdot \frac{\left[1 + 2\Lambda/c - \sqrt{(1+2\Lambda/c)^2 - 1}\right]^n}{\sqrt{(1+2\Lambda/c)^2 - 1}} d\Lambda, \tag{2.26}$$

where (2.1), with $\phi = \omega t$, is time integrated to obtain $W(t) = \int u_s(t)dt = u_s(t - \frac{\sigma}{\omega}\cos(\omega t))$. Furthermore, (2.26) is rearranged and the definition of the reduced frequency k is used to obtain

$$b_n(t) = -\frac{2}{\pi c} \sum_{m=-\infty}^\infty a_m im \frac{2k}{c} e^{im(\omega t - \sigma \cos(\omega t))}$$
$$\cdot \int_0^\infty e^{-im\frac{2k}{c}\Lambda} \frac{\left[1 + 2\Lambda/c - \sqrt{(1+2\Lambda/c)^2 - 1}\right]^n}{\sqrt{(1+2\Lambda/c)^2 - 1}} d\Lambda. \tag{2.27}$$

The coefficient a_m is already determined in general in (2.20) and $S_m = im(2k/c)\exp[im(\phi - \sigma\cos(\phi))]$ is introduced. The substitution $\Lambda = c\,\tilde{\Lambda}$ with $d\Lambda = c\,d\,\tilde{\Lambda}$ simplifies the final equation and the phase angle $\phi = \omega t$ is introduced for simplification, without loss of generality, to give

$$b_n(\phi) = -\frac{2}{\pi} \sum_{m=-\infty}^\infty A_m S_m \frac{\int_0^\infty e^{-imk2\tilde{\Lambda}} \frac{\left[1+2\tilde{\Lambda}-2\sqrt{\tilde{\Lambda}^2+\tilde{\Lambda}}\right]^n}{2\sqrt{\tilde{\Lambda}^2+\tilde{\Lambda}}} d\tilde{\Lambda}}{1 + 2imk \int_0^\infty e^{-imk2\tilde{\Lambda}} \left(\sqrt{\frac{1}{\tilde{\Lambda}} + 1} - 1\right) d\tilde{\Lambda}}. \tag{2.28}$$

Now, the problem of the unsteady bound vortex sheet $\gamma_b(\Theta, t)$ is completely solved using the integrals given in the Appendix of Strangfeld *et al.* (2016). By means of the known coefficients b_n, $\gamma_b(\Theta, t)$ is determined for all arbitrary amplitudes σ and reduced frequencies k. Although A_m, S_m and the denominator in (2.28) are independent of n, the integral in the numerator possesses n as an exponent. Thus, for all desired wavenumbers m and coefficients b_n, this equation has to be solved separately. This results in excessive processing time because several hyperbolic Bessel functions K and confluent hypergeometric Kummer functions M are part of the solution. Exact solutions of the integrals of the first eight coefficients are given in Strangfeld *et al.* (2016) for arbitrary σ and k. Finally, this explicit formulation of the bound vortex sheet enables the determination of the two contributions to lift, namely the Joukowsky and impulsive-pressure contributions, expressed below as coefficients

$$C_{L,j}(t) = \frac{2}{u(t)} \int_{-0.5}^{0.5} \gamma_b(\bar{x}, t)d\bar{x}, \tag{2.29}$$

and

$$C_{L,i}(t) = \frac{2c}{u^2(t)} \frac{d}{dt} \int_{-0.5}^{0.5} \gamma_b(\bar{x}, t)(0.5 - \bar{x})d\bar{x}. \tag{2.30}$$
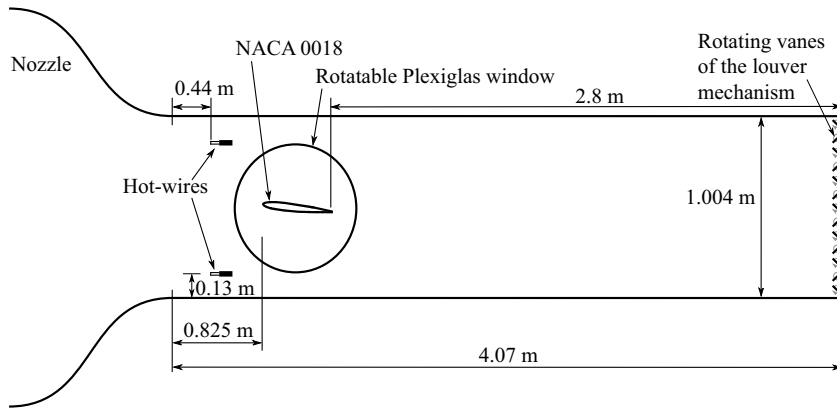
Figure 2. Schematic of the the wind tunnel set-up. The airfoil is rotated about its quarter-chord location and surging is achieved by periodically opening and partially closing the louver vanes at the downstream end of the test section. The unsteady free-stream velocity is recorded upstream of the airfoil by means of two hot-wire probes mounted near the floor and ceiling of the tunnel.

Equations (2.29) and (2.30) are particularly useful for evaluating experimental data where the bound vortex sheet strength can be measured directly. They are also useful for identifying the source of deviations of experimental data from theory.

In summary, the approach presented in this section obviates the need for integral formulations of the bound vortex sheet, which are generally used to calculate the unsteady circulation and lift. The bound vortex sheet strength is affected by the oscillating free stream and unsteady pitching motion, as well as by the shedding of wake vortices at the trailing edge. The entire wake vortex sheet induces normal velocities on the airfoil which leads to an infinite summation of the coefficients $c_n = b_{n+1} - b_{n-1}$, as shown in (2.25). This summation is done by the explicit formulation of b_n in (2.28) that leads to the computation of the bound vortex sheet strength at all chord positions, including the trailing edge. The shed wake vortices also induce normal velocities at the trailing edge of the airfoil. Thus, in order to satisfy the Kutta condition under unsteady conditions, the bound vortex sheet strength at the trailing edge must have non-zero values to compensate for the induced normal velocities.

3. Experimental set-up

Experiments were performed employing a NACA 0018 airfoil model in the Technion's unsteady low-speed wind tunnel (Greenblatt 2016). It is driven by a speed-controlled 75 kW centrifugal blower, with an 8:1 nozzle contraction ratio and a 0.61 m × 1.004 m test-section area (see figure 2). The maximum free-stream velocity u_s is 55 m s^{-1} with a turbulence level of less than 0.1 %. The ceiling, floor and sidewalls of the test section are constructed from Plexiglas. The tunnel exit is equipped with 13 fully rotatable louver vanes, driven by a 0.75 kW servo motor, that control the tunnel surging flow with a maximum area blockage of 95 %. The tunnel frequency bandwidth, or cutoff, was determined theoretically and experimentally to be

$$f_c = \frac{1}{2\pi} \left(\frac{A}{\bar{A}_e} \right)^2 \frac{u_s}{L_{ts}}, \qquad (3.1)$$

where $A/\bar{A}_e$ is the ratio of the test-section area to the mean open exit area and L_{ts} is the test-section length. These two parameters, which are variable, were 1.90 and

1009 A41-10

4.07 m, respectively, for the present experiments, to yield $f_c = 1.87$ Hz (or $k_c = 0.15$). Experiments were performed with relative surging amplitudes $\Delta u/u_s \leqslant 0.51$, and because the cutoff frequency scales linearly with the mean tunnel speed, changes to the test frequency have no effect on $\Delta u/u_s$.

The airfoil ($c = 0.348$ m) was mounted rigidly at the vertical centre of the test section, between two rotatable Plexiglas windows, each with a diameter of 0.93 m. The pitch axis was located at the quarter-chord point and the leading edge was positioned 0.825 m downstream of the nozzle. Synchronous pre-stall harmonic pitching – at arbitrary phase differences τ relative to surging – was achieved using a 1.5 kW servo-motor, located above the test section, via a 1:150 belt system attached to the windows. The instantaneous angle-of-attack was measured independently using an optical encoder, where the difference between the commanded and measured values never exceeded $\pm 0.2°$. The unsteady free-stream velocity in the test section was measured by averaging the signals of two hot-wire probes, mounted above and below the airfoil, attached to an AN-1003 Hot-Wire Anemometry System (A.A. Lab Systems). The anemometer has a cutoff frequency of 120 kHz, and for all signals acquired here a 5 kHz low-pass filter was enforced (more details can be found in Appendix A.2). Calibrations were performed with a Pitot-static (Prandtl) tube and Dwyer manganese pressure transducer. The airfoil was equipped with 40 symmetrically disposed pressure ports (0.8 mm diameter), designated p_l ($l = 1, \ldots, 40$) – closely spaced near the leading edge in order to capture the large pressure gradients – and coupled to two piezoresistive pressure scanners (SP-32HD, TE Connectivity) via 44 cm long tubes. The pressure lag and amplitude attenuation were found to be negligible for the maximum oscillation frequencies of 1.2 Hz considered here (cf. Greenblatt *et al.* 2001; Nagib *et al.* 2001). The data acquisition of the surface pressures and the wind tunnel speed were synchronised, acquired at a frequency of $f_{daq} = 497$ Hz and phase averaged to obtain $p_l(x, \phi)$ and $u(\phi)$. Uncertainties associated with individual pressure coefficient measurements $\Delta C_{p,l}$ never exceeded 0.0047 based on 99.7 % confidence intervals (see Appendix A.1). Wind tunnel blockage corrections were not implemented, due to the low angles-of-attack ($\alpha_{max} = 4°$) considered and resulting low maximum blockage ratio of 8.7 %. Furthermore, lift coefficient ratios (see (2.3)), vortex sheet differences and form-drag coefficient ratios are considered here, which eliminates any potential wind tunnel bias.

The measured static pressure, which acts normal to the surface, was weighted by the half-distance to the neighbouring pressure taps and transformed in the coordinate system of the wing chord. Summations were then employed to obtain the lift force and the form-drag force. The cross-product of the static pressure at each pressure port and the distance to the quarter-chord were used to obtain the pitching moment. It was recently recognised by Greenblatt *et al.* (2023) that, because surging flows produce streamwise temporal pressure gradients, the local measured static pressure in the wind tunnel $p_{st} = p_{st}(x, \phi)$ must be used to calculate the surface-pressure coefficients $C_p(x, \phi)$. Assuming incompressible flow and harmonic surging, Greenblatt *et al.* (2023) showed that the pressure coefficients must be calculated according to

$$C_{p,l}(x', \phi) = \frac{p_l(x', \phi) - p_{st}(0, \phi)}{q(\phi)} + 4\sigma k \hat{x} \frac{\cos \phi}{(1 + \sigma \sin \phi)^2}, \qquad (3.2)$$

where x' is measured from the airfoil leading edge, $q(\phi) = 1/2 \rho u^2(\phi)$ is the tunnel dynamic pressure and $\hat{x} = x'/c$. The correction term in (3.2) (second term on the right) brings about either no difference ($\alpha = 0°$) or near negligible differences ($\alpha \neq 0°$) to C_l and C_m due to the correction being applied on both surfaces. However, the correction term
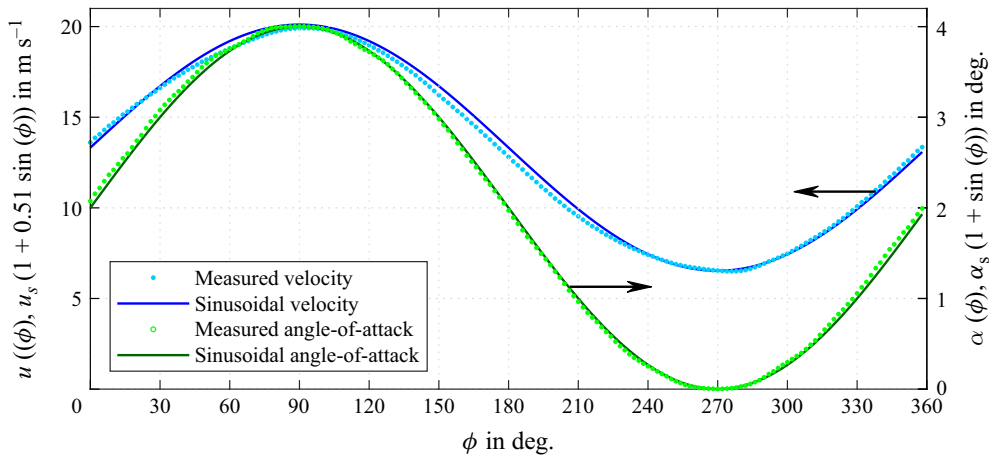
Figure 3. Comparison of the measured free-stream velocity (blue dots) and measured angle-of-attack (green dots) with the sinusoidal functions $u(\phi) = (1 + 0.51\sin(\phi))13.32$ m s^{-1} and $\alpha(\phi) = 2° + 2°\sin(\phi)$ depicted by solid lines. Arrows indicate corresponding ordinates.

brings about enormous changes to the form-drag coefficient C_{dp}, which otherwise exhibits large non-physical positive and negative oscillations.

To summarise, an unsteady wind tunnel was used to perform synchronous high-amplitude surging and pre-stall pitching experiments on a NACA 0018 airfoil. High-precision airfoil surface-pressure and wind tunnel velocity measurements were made. Resulting high-precision phase-averaged pressure coefficients were corrected for streamwise temporal pressure gradients.

4. Results and discussion

4.1. *Surging and pitching wind tunnel conditions*

An example of synchronous in-phase ($\tau = 0°$) free-stream velocity and angle-of-attack measurements is shown in figure 3 for $u_s = 13.32$ m s^{-1}, $\sigma = 0.51$, $\alpha(\phi) = 2° + 2°\sin(\phi)$ and $k = 0.097$. Free-stream velocities are based on the phase-averaged hot-wire measurements near the wall and ceiling and angles-of-attack are phase-averaged shaft encoder data. Each phase-averaged data set consists of $N = 1328$ periods of the unsteady cycle, where averaging is performed at ϕ steps of $2°$ with a window size of $\pm 1°$ (see Appendix A for more details). In addition, each of the data sets is represented by an ideal sine wave determined from a least-squares approximation, which serves two purposes. First, it provides representative approximations for the theoretical calculations and, second, it allows us to quantify experimental deviations from idealised conditions. The largest detectable deviations are around phase angles $\phi = 60°$ and $\phi = 180°$, with a 2.5 % maximum relative error between the measured free stream and the idealised sine function (also see Strangfeld *et al.* 2014). The maximum and the minimum values exhibit small phase lags of approximately $4°$ while the crossing of the steady free-stream velocity shows a phase lead of approximately $-4°$. The measured angle-of-attack data produced $\alpha_s = 2.00°$ and $\alpha_a = 2.01°$ and the measured angle-of-attack corresponded well with a least-squares sine wave. Furthermore, a computed cross-correlation between the measured angle-of-attack and the measured velocity profile exhibited a phase lag of $0.0°$. Finally, hot-wire probes mounted at $1.1c$ upstream and downstream of the leading and trailing edges, respectively, indicated that, at the test frequency $f = 1.18$ Hz, phase lag due to

compressibility effects was small, i.e. $\Delta\phi \leqslant 1°$. Thus, the incompressibility condition was not violated.

Justification for the parameters selected here, namely $k = 0.097$, $\sigma = 0.51$ and $\alpha(\phi) = 2° + 2° \sin(\phi)$, is based on the idealised flowfield encountered by the nominally rigid blades of high-speed co-axial helicopters (see Barbely & Komerath 2016; Feil *et al.* 2020; Singh & Friedmann 2021). These blades experience synchronous high-amplitude velocity oscillations, together with synchronous pre-stall angle-of-attack oscillations that arise due to aeroelasticity and interactions between the rotors. Consider the idealised in-plane velocity magnitude distribution parallel to the chord-line (Lind *et al.* 2016), written as

$$V_{||} = V\hat{r}[1 + (\mu/\hat{r})\sin(\psi)], \tag{4.1}$$

where $\hat{r} = r/R$ is the dimensionless distance from the hub to the tip, and ψ is azimthal angle around the rotor. By comparing (4.1) and (2.1), it is clear that the two-dimensional representation of the rotor assumes that $\omega \equiv \Omega$, $u_s \equiv V\hat{r}$, $\sigma \equiv \mu/\hat{r}$ and $\psi = \phi$. The global reduced frequency encountered at an arbitrary radial location along the blade span can therefore be expressed as

$$k = \frac{\Omega c}{2V\hat{r}} = \frac{1}{2\mu}\frac{c}{r}. \tag{4.2}$$

Helicopter blade aspect ratios R/c typically vary between 15 and 20 (Conlisk 2001), and because we are mainly interested in the lift-producing outer half of the blades, we take $r/c = 7.5$ as our lower limit. Rearranging (4.2) and substituting $k = 0.097$, results in $\mu = 0.69$ and 0.51 for $r/c = 7.5$ and 10, respectively, which are typical for high-speed co-axial helicopters (Lind *et al.* 2016; Feil *et al.* 2020). Our choice of $\sigma = 0.51$ is consistent with the conditions encountered at the blade tips, i.e. $\mu = \sigma = 0.51$. The angle-of-attack variation throughout the cycle remains pre-stall by design, and for the purposes of this investigation, the phase relation between surging and pitching is left as the free parameter τ, as shown in (2.8).

4.2. *Pure surging and pure pitching*

Quasi-steady and unsteady lift coefficients, relative to their average, namely $C_l(\phi)/C_{l,s}(\alpha = 2°)$, are shown for both pure pitching and pure surging experiments (dots), together with corresponding theory (dashed lines), in figure 4. Quasi-steady pitching data at $Re_s = 3.0 \times 10^5$ were generated by pitching the airfoil at $k = 0.0005$, i.e. more than two orders of magnitude slower than the unsteady case. Surprisingly, the quasi-steady pitching data do not correspond to elementary steady theory, and there are two reasons for this. First, the geometric zero angle-of-attack $\alpha = 0°$ produces a small offset, namely $C_l(\alpha = 0°) = 0.019$, due to a slight asymmetry caused by the slots. Second, the lift slope is less than the theoretical value, namely $dC_l/d\alpha \approx (0.91)2\pi$, due to a combination of the relatively thick airfoil and relatively low Reynolds number. Hence, the quasi-steady $C_l(\phi)/C_{l,s}(\alpha = 2°)$ data presented in figure 4 do not go to zero when $\alpha = 0°$ and do not equal 2 when $\alpha = 4°$.

For the pure unsteady pitching case, the correspondence between the data and theory of Theodorsen (1935), indicated by the green dashed line, is excellent. Additionally, the data were filtered by summing the first two terms of their Fourier series (solid green line). The excellent correspondence is somewhat misleading because the changes between the quasi-steady and unsteady theories are larger than those observed in the experiments. In both theory and experiments, the respectively low and high lift coefficients at $\phi \approx 90°$ and 270°, relative to quasi-steady theory, are principally due to wake circulation effects (Motta, Guardone & Quaranta 2015). It is likely that the effect observed in the experiments
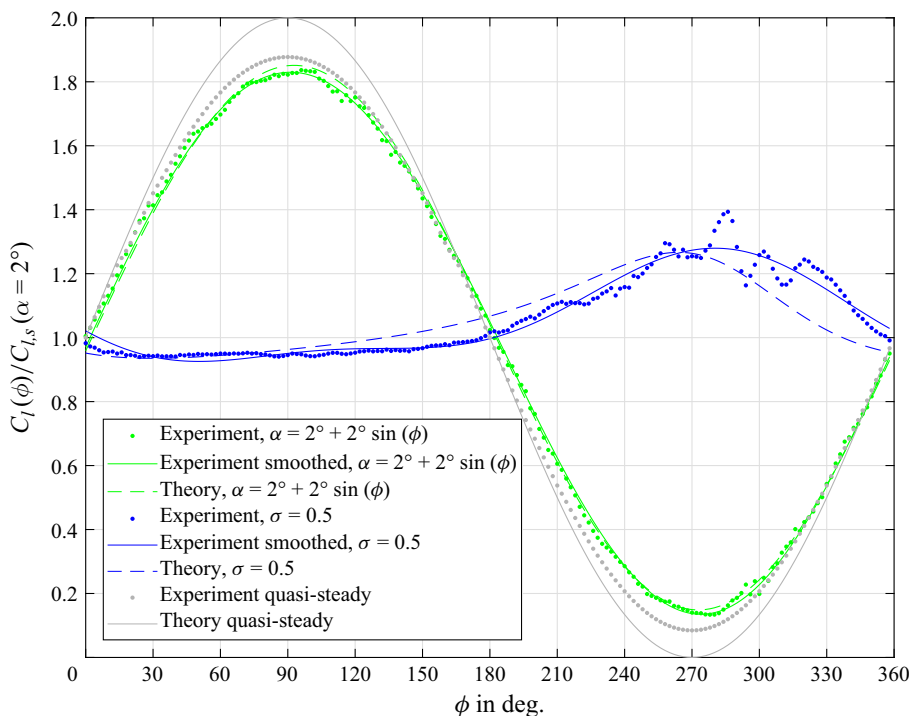
Figure 4. Comparison of experiment and theory for the ratio of unsteady to quasi-steady lift coefficients under pure surging (theory of Isaacs 1945) with $\sigma = 0.51$ and under pure pitching (theory of Theodorsen 1935) with $\alpha(\phi) = 2° + 2° \sin(\phi)$ at $Re_s = 3.0 \times 10^5$ and $k = 0.097$.

is smaller due to the finite boundary layer thicknesses at the trailing edge. This assumption is based on the difference between the theoretically imposed Kutta condition and the *de facto* experimental induced velocities at the trailing edge. Namely, in the theory, the wake is assumed to be flat with zero thickness, while in experiments, the wake thickness is determined by the sum of the the boundary layer thicknesses on both surfaces. The data shown in the figure are sometimes presented as counter-clockwise (phase lag) C_l versus α, hysteresis loops, but the present phase-dependent representation is clearer. Non-circulatory apparent mass effects are not a significant factor, because they only become important at much higher reduced frequencies. Theoretically, at $k = 0.144$ a phase inversion occurs, meaning that the hysteresis loops switch from counter-clockwise to clockwise. Motta *et al.* (2015) also showed theoretically, that the phase inversion increases with the airfoil thickness because the potential difference across the airfoil is affected by finite airfoil thickness. In particular, at reduced frequencies less than the phase-inversion point, $d\alpha/dt > 0$ brings about an increment of the kinematic angle-of-attack, which increases the phase lag to produce wider counter-clockwise hysteresis loops. Nevertheless, theoretical differences between a flat plate airfoil and a NACA 0018 airfoil at $k = 0.097$ are relatively small, namely $\Delta C_l \approx 0.01$.

Quasi-steady surging data were generated by performing quasi-steady pitching experiments, described above, at 11 free-stream velocities between $(1 - \sigma)u_s$ and $(1 + \sigma)u_s$ and then extracting the data points at $\alpha = 2°$. Then, data corresponding to unsteady free-stream velocities were interpolated from the constant velocity data. Thus, Reynolds number effects, which were relatively minor, were implicitly accounted for in the $C_l(\phi)/C_{l,s}(\alpha = 2°)$ unsteady surging results presented (see Appendix A.1 for more

details). These data were also filtered by summing the first two terms of their Fourier series (solid line) and the pure unsteady surging theoretical result of Isaacs (1945) is shown as a dashed line. Overall, the data capture the phase lag associated with a delay in the development of lift as well as the slightly lower lift coefficient at maximum velocity predicted by Isaacs (1945). However, the data lag the theoretical result during the deceleration phase ($\mathrm{d}u/\mathrm{d}t < 0$), where there is a lift overshoot. This may be due to airfoil thickness effects, analogously to the analysis of Motta *et al.* (2015) described above, where increasing airfoil thickness increases phase lag when compared with flat plate theory. More likely, it is an effect of the finite boundary layer thicknesses at the trailing edge as described above. Unlike the pure pitching case, surging produces relatively high-frequency oscillations at the beginning of the acceleration phase, i.e. following $\phi > 270°$. Greenblatt *et al.* (2023) showed evidence that this was due to bubble bursting, surprisingly occurring during early stages of the acceleration ($\partial p/\partial x < 0$), because the favourable pressure gradient rapidly drives upper and lower surface separation bubbles aft, rendering them unable to reattach to the airfoil surfaces.

The bubble-bursting mechanism described here is different to 'conventional' LSB bursting, for example, described by Gaster (1967). Conventional bursting is predicted by a pressure gradient parameter based on the inviscid pressure rise across the bubble, that appears as the negative term $\Delta u_p/\Delta x$ in Gaster's criterion, where u_p is the surface potential flow velocity. If we generalise Gaster's criterion to include unsteady surging effects, then we should consider the equivalent pressure gradient term $u_p^{-1}\partial u_p/\partial t$. Note, however, that this term is negative for $90° < \phi < 270°$, where no bubble bursting is observed. Therefore Gaster's criterion is not applicable here. Rather, the assumed bubble bursting observed in our data is due mainly to the downstream movement of the separation point due to the favourable pressure gradient, such that it cannot reattach to the surface, as described by the integral analysis of Greenblatt *et al.* (2023).

Note that the high-frequency oscillations are characterised first by an increase and then a decrease in the lift coefficient. We hypothesise that, because the lower surface bubble separation point is further downstream, it bursts first. Bursting produces a local region of low pressure just downstream of, and below, the trailing edge, which deflects the trailing-edge streamlines downwards, thereby causing a momentary increase in lift. This is followed by bursting of the upper surface bubble that has the opposite effect of decreasing lift. Hence, the order of bubble bursting is responsible for the high-frequency lift coefficient oscillations observed in the data during the early part of the free-stream acceleration. Violation of the classical steady-flow Kutta condition observed by Zhu *et al.* (2020) may be related to this assumed bubble-bursting phenomenon, but this is merely speculation at this point.

4.3. *In-phase surging and pitching*

The lift force $L(\phi)$ acting on the airfoil is proportional to both dynamic pressure $q(\phi)$ and angle-of-attack $\alpha(\phi)$. Therefore, we can expect to observe the greatest nonlinear effects when pitching and surging are in phase, i.e. at $\tau = 0$. Synchronous in-phase surging-and-pitching results for the conditions described in the previous section, i.e. $Re_s = 3.0 \times 10^5$ and $k = 0.097$, are shown in figure 4. The close correspondence between the data and van der Wall's theory suggests that the theory adequately captures the dominant unsteady effects of synchronous surging and pitching. Note, furthermore, that the effect on the lift coefficient due to synchronous surging and pitching is not merely the superposition of their individual contributions. This is made evident by superimposing the results of Isaacs (1945) and Theodorsen (1935) and is shown as the red line in figure 4, which
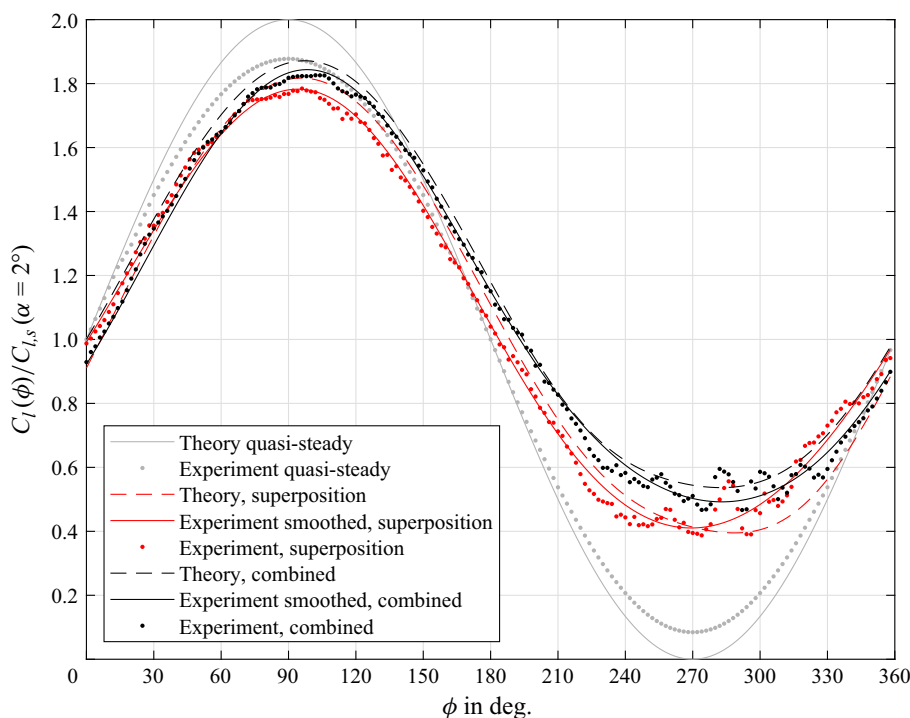
Figure 5. Comparison of experiment and theory for the ratio of unsteady to quasi-steady lift coefficients under synchronous surging and pitching with $\sigma = 0.51$, $\alpha(\phi) = 2° + 2° \sin(\phi)$ and $\tau = 0°$ at $Re_s = 3.0 \times 10^5$ and $k = 0.097$. Unsteady theory is due to van der Wall (1991) and superposition refers to the theories of Theodorsen (1935) and Isaacs (1945) are shown.

falls below the theoretical prediction of van der Wall (1991). An identical superposition exercise was performed using the individual experimental data sets, shown as the red dots, and a similar result was obtained. The difference between synchronous surging and pitching and the superimposed result is due to variation in the phase-dependent 'effective reduced frequency' experienced by the airfoil during pitching. For superposition, the reduced frequency is simply $k = \omega c / 2u_s$, but with synchronisation it is $k_e(\phi) = \omega c / 2u(\phi)$, e.g. 1.5 times lower and higher at $\phi = 90°$ and $270°$, respectively. Note, furthermore, that the high-frequency lift oscillation, caused by bubble bursting, is also present during combined surging and pitching. This suggests that the bubble-bursting mechanism is not materially affected when the free-stream velocity and angle-of-attack are in phase.

4.4. *Effect of phase difference*

The in-phase pitching-and-surging case with $\sigma = 0.51$, described in the previous section, resulted in relatively large effects on the lift coefficient. In this section, we extend the validation to include lower surging amplitude cases ($\sigma = 0.33$ at $k = 0.08$) as well as angle-of-attack phase-lead angles $\tau = 90°$, $180°$ and $270°$. Note that the latter two phase differences represent idealised conditions experienced by helicopter rotor blades in forward flight and vertical axis wind turbine blades, respectively. A summary of the experimental results, together with quasi-steady theory and the theory of van der Wall (1991), is presented in figure 6, where four blocks of three vertically stacked images represent the four phase differences τ supplementary movies 1 and 2. Measurements of the normalised free-stream velocity $u(\phi)/u_s$ (red and green lines) and angle-of-attack
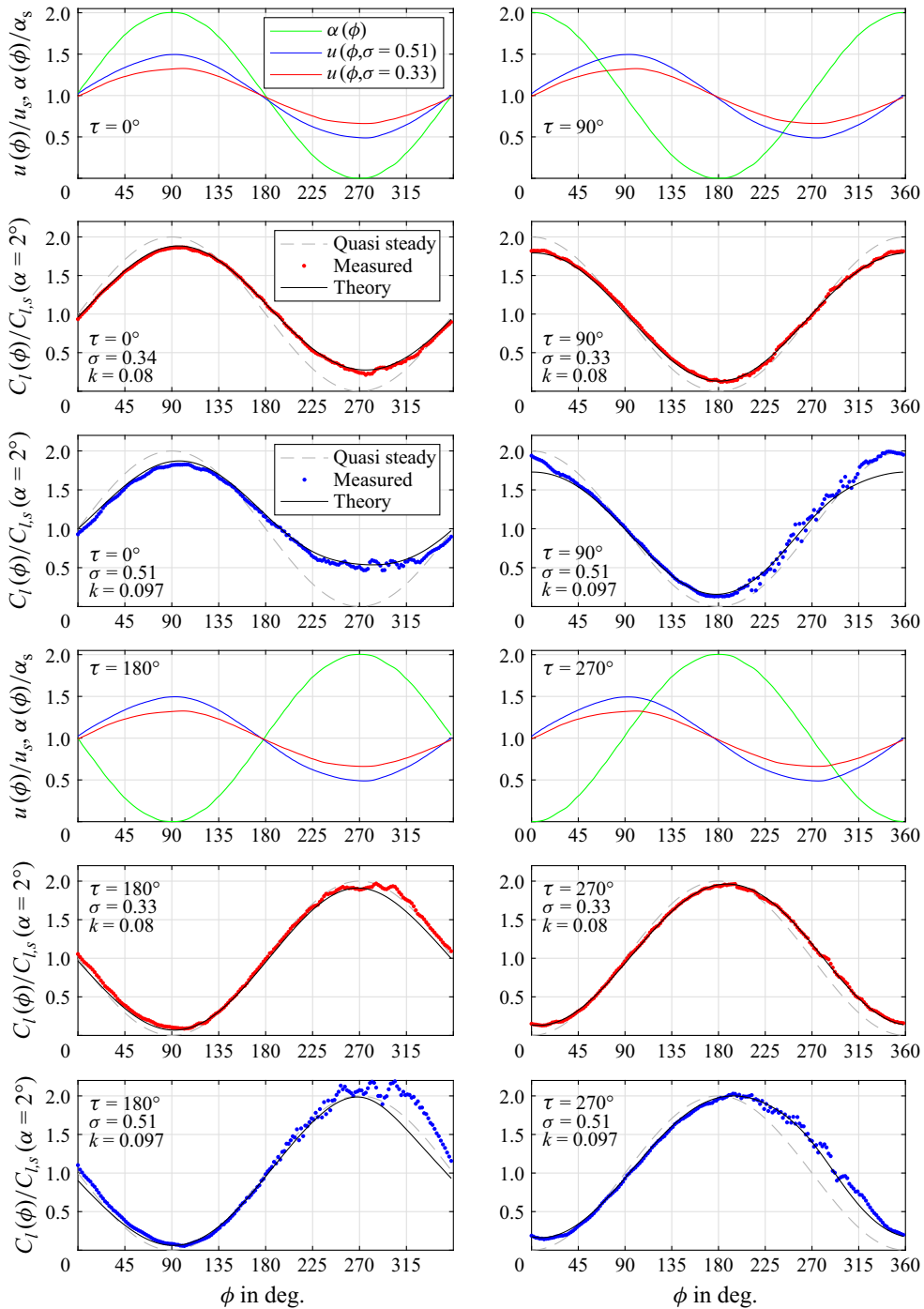
Figure 6. Measured and theoretical unsteady lift coefficient ratios under synchronous surging and pitching at $\alpha(\phi) = 2° + 2° \sin(\phi + \tau)$, for phase angles $\tau = 0°$, $90°$, $180°$ and $270°$; red and green symbols correspond to $\{\sigma, k\} = \{0.33, 0.08\}$ and $\{0.51, 0.097\}$, respectively supplementary movies 1 and 2.

$\alpha(\phi)/\alpha_s$ (blue lines) are shown (see the methods described in § 3). For the lower surge-amplitude case ($\sigma = 0.33$, $k = 0.08$), with the exception of $\tau = 180°$, the correspondence between data and theory is excellent. The possible reasons for the deviations at $\tau = 180°$ are discussed below. The high-frequency oscillations previously observed at $\tau = 0°$ in the vicinity of $270° < \phi < 330°$ are significantly ameliorated, which indicates a change to the assumed bubble-bursting mechanism. There appear to be two possible effects of the smaller free-stream oscillation amplitude. First, the separation points do not move as far downstream due to the weaker temporal pressure gradient; and second, the minimum Reynolds number is higher, which also renders the bubbles less likely to burst.

At $\tau = 90°$, the velocity maximum and minimum correspond to peak negative and positive pitch rates, $(d\alpha/dt)_{min}$ and $(d\alpha/dt)_{max}$, respectively. For the higher-amplitude case, correspondence is excellent for $45° < \phi < 315°$ but a breakdown is observed outside of these bounds. The most likely reason for this is the combination of relatively low Reynolds number combined with the pitch-up motion, that exacerbates bubble bursting (see § 4.6). This hypothesis is reinforced by considering the comparison at $\tau = 180°$, where the velocity and angle-of-attack are in anti-phase, i.e. the lowest Reynolds number corresponds to the highest angle-of-attack. Another factor that affects the correspondence between experiment and theory is the relative contributions of the Joukowsky and impulsive-pressure components of lift generation, and this is discussed below. The anti-phase relation is of particular interest, because it is an idealised representation of the flow encountered by a co-axial helicopter blade of a helicopter in forward flight. Therefore the propensity of the bubble to burst under these conditions– which is effectively low angle-of-attack dynamic stall– can have important consequences for rotor performance and noise. In light of the fact that co-axial rotors are designed specifically to mitigate the adverse effects of retreating blade stall, this potentially new 'dynamic stall' mechanism may adversely impact rotor performance, and should be taken into consideration. In terms of aeroacoustics, the interaction between the turbulent boundary layer with the rotor blade trailing-edge discontinuity, typically modelled by the Kutta condition, causes turbulent energy to be scattered as far-field noise in a dipolar pattern (Lee *et al.* 2021). Therefore, if the Kutta condition is violated by dynamic stall precipitated by bubble bursting on one or both surfaces, for example during forward flight (cf. $\tau = 180°$), this will affect the noise scattering. At $\tau = 270°$, the minimum velocity corresponds to the maximum pitch-down rate $(d\alpha/dt)_{min}$ (cf. $(d\alpha/dt)_{max}$ at $\tau = 90°$). Here, the correspondence improves, most probably because the pitch-down motion is less likely to produce bubble bursting.

The theories of Isaacs (1945) and van der Wall (1991) are limited somewhat in that they provide only circulatory and non-circulatory loads acting on the airfoil. Consequently, they do not provide the explicit vortex sheet distribution γ; neither do they distinguish between the Joukowsky lift and impulsive-pressure lift contributions. Both of these factors are important for experimental validation of the theory because the vortex sheet strength can be estimated directly from the airfoil pressure measurements and the different contributions to lift generation assist in interpreting the experimental data. Note that overall unsteady loads can be thought of as either the sum of the circulatory and non-circulatory lift components (see (2.3)) or as the sum of Joukowsky lift and the impulsive-pressure lift components (see (2.29) and (2.30)). To illustrate this, the bound unsteady vortex sheet was computed for each phase angle under the conditions $\alpha(\phi) = 2° + 2° \sin(\phi + \tau)$, $\sigma = 0.51$ and $k = 0.097$, and then integrated numerically to obtain $C_{L,j}$ and $C_{L,i}$. These coefficients were then non-dimensionalised with respect to the steady-state values at $\alpha = 2°$ and presented together with the similarly non-dimensionalised circulatory and non-circulatory lift coefficient components shown in figure 7 for $\tau = 0°$ as a function of phase angle. The difference between circulatory lift
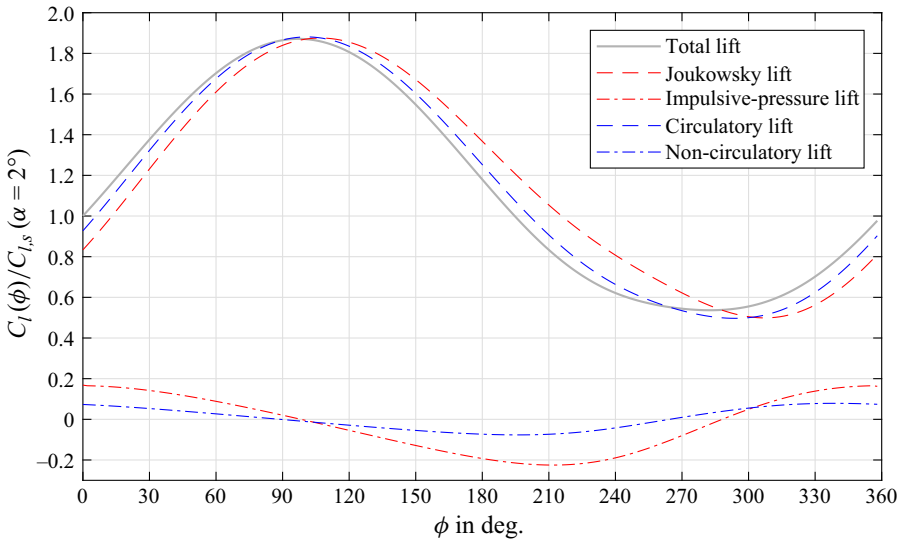
Figure 7. Presentation of the non-dimensionalised individual lift coefficient components as a function of phase angle for $\tau = 0°$. The sum of the former two and the latter two produce the overall loading developed by Isaacs (1945).

and Joukowsky lift is that the latter integration does not explicitly take wake effects into account and is the same integration as that performed in a steady flow. The difference between the non-circulatory and impulsive-pressure lift is that the former is proportional to the time derivative of the free-stream velocity, while the latter is proportional to the time derivative of the integrated bound vortex sheet weighted by distance from the leading edge. Note that the sum of both component pairs, i.e. the overall aerodynamic loading predicted by van der Wall, is virtually identical for both cases, with maximum differences not exceeding 0.56 %. These small differences are caused partly by the numerical integration and partly because the Kutta condition cannot be perfectly imposed numerically at the trailing edge (see discussion below).

Comparisons between experimental data and theory are shown in figure 8 for $\tau = 0°$ and 180°, where the black solid lines are the unsteady lift prediction of van der Wall as described in (2.3) and the green solid lines represent the integration of the bound unsteady vortex sheet according to (2.29) and (2.30). The in-phase and anti-phase results illustrate the relative importance of the Joukowsky and impulsive-pressure lift contributions, that are also shown in the figures. In the case of pure surging described by Strangfeld *et al.* (2016), the maximum positive-lift and negative-lift impulsive-pressure component leads and lags the accelerations by approximately $\Delta\phi \approx 30°$, respectively. For pure pitching the impulsive pressure is almost perfectly in phase with the accelerations, due to the relatively small $k \approx 0.1$. Therefore, because the surging-and-pitching impulsive-pressure contributions are almost in phase when $\tau = 0°$ (figure 8a), their combined contribution to the overall lift is large. In fact, the differences between the quasi-steady and unsteady Joukowsky lift effects and the impulsive-pressure effects are comparable in magnitude. Now, because bubble bursting primarily affects the experimental component of Joukowsky lift, its effect on the overall lift at $\tau = 0°$ results in relatively small maximum deviations from theory, namely $\Delta C_l \approx 0.1$. In contrast, at $\tau = 180°$, where the Joukowsky lift makes up virtually the entire contribution, the maximum deviations are much larger, namely $\Delta C_l \approx 0.5$. Here, the impulsive-pressure contributions due to pitching and surging, whose
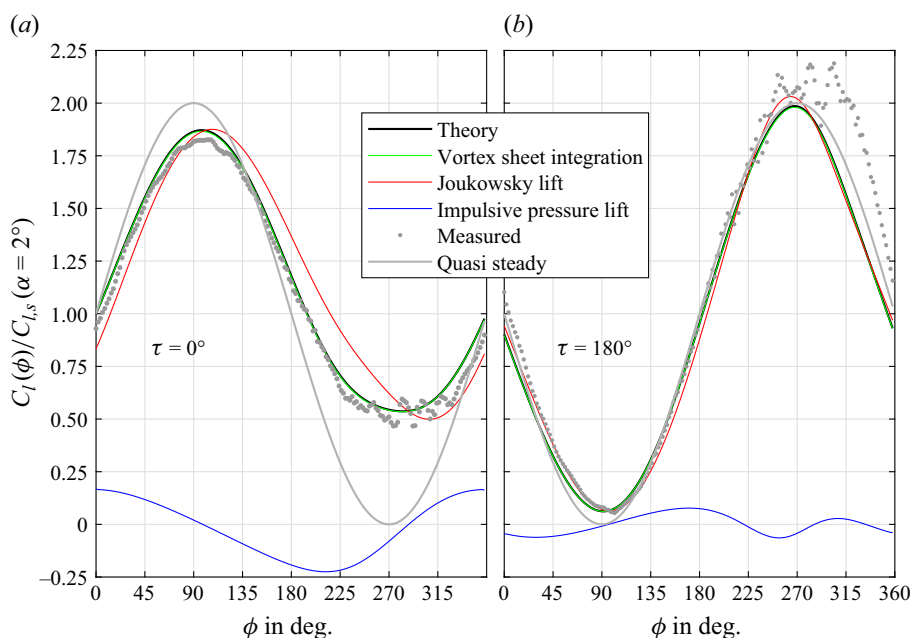
Figure 8. Illustration of the different contributions to unsteady lift, based on the theory of van der Wall (1991) and integration of the bound unsteady vortex sheet, under synchronous surging ($\sigma = 0.51$) and pitching ($\alpha(\phi) = 2° + 2° \sin(\phi + \tau)$) for $\tau = 0°$ and $180°$, at $Re_s = 3.0 \times 10^5$ and $k = 0.097$.

integrands are weighted by distance from the leading edge, are close to anti-phase and their net effects are small throughout the cycle. This is illustrated in figure 8b, which shows that, at $\tau = 180°$, the impulsive-pressure lift contribution is negligible. Therefore, because the bubble bursting predominately affects the Joukowsky lift, the experimental lift coefficient data show a relatively large departure from theory.

4.5. *The bound unsteady vortex sheet*

The close correspondence between the numerically integrated unsteady vortex sheet (2.29) and (2.30) and the theoretical unsteady lift prediction (2.3), implies that we can confidently rely on our theoretical results and compare them with the experimentally generated bound vortex sheet strengths. Experimentally, the vortex sheet strength is calculated across corresponding high-pressure and low-pressure surface port locations (i.e. corresponding to the same x_l') according to $\gamma_{b,l} = \Delta p_l / (\rho u(t))$. For the quasi-steady representation $\gamma_{b,l,qs}$, the quasi-steady pressure differences are used and $u(t)$ is replaced with the corresponding u_s. The theoretical unsteady and quasi-steady bound vorticities are calculated according to (2.25) and (2.28) and according to Anderson (2011), respectively.

A comparison of non-dimensional theoretical and experimental unsteady vortex sheet strengths is shown in figure 9 for all four phase leads. The correspondence between theory and experiment is generally good for $\hat{x} \lesssim 0.5$, with two main exceptions. First, the experimental peak values near the leading edge are somewhat lower than the theoretical values, and second, marked deviations from theory are observed along the trailing edge and at localised regions upstream of the trailing edge. A primary reason for the lack of correspondence at the trailing edge is because the unsteady vortex sheet does not tend to zero as $\hat{x} \to 1$. For both steady and unsteady cases, the wake vortices induce normal velocities on the vortex sheet and hence the vortex sheet strength must be adjusted such that
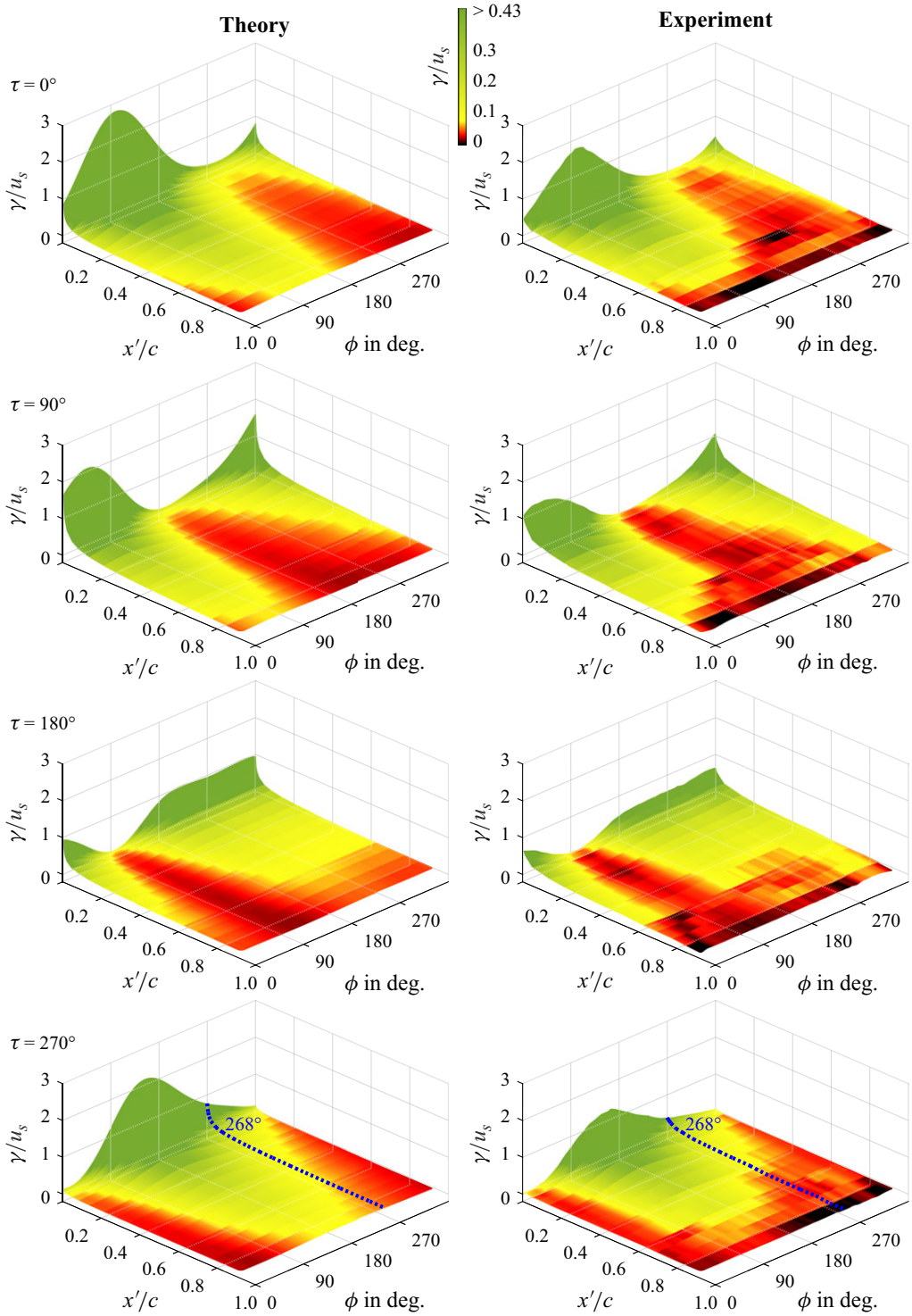
Figure 9. Non-dimensional theoretical and experimental unsteady vortex sheet strengths γ/u_s along the normalised airfoil chord x'/c as a function of phase ϕ, corresponding to $\sigma = 0.51$, $k = 0.097$, $Re_s = 3.0 \times 10^5$ and $\alpha(\phi) = 2° + 2° \sin(\phi + \tau)$, for the four phase angles τ.
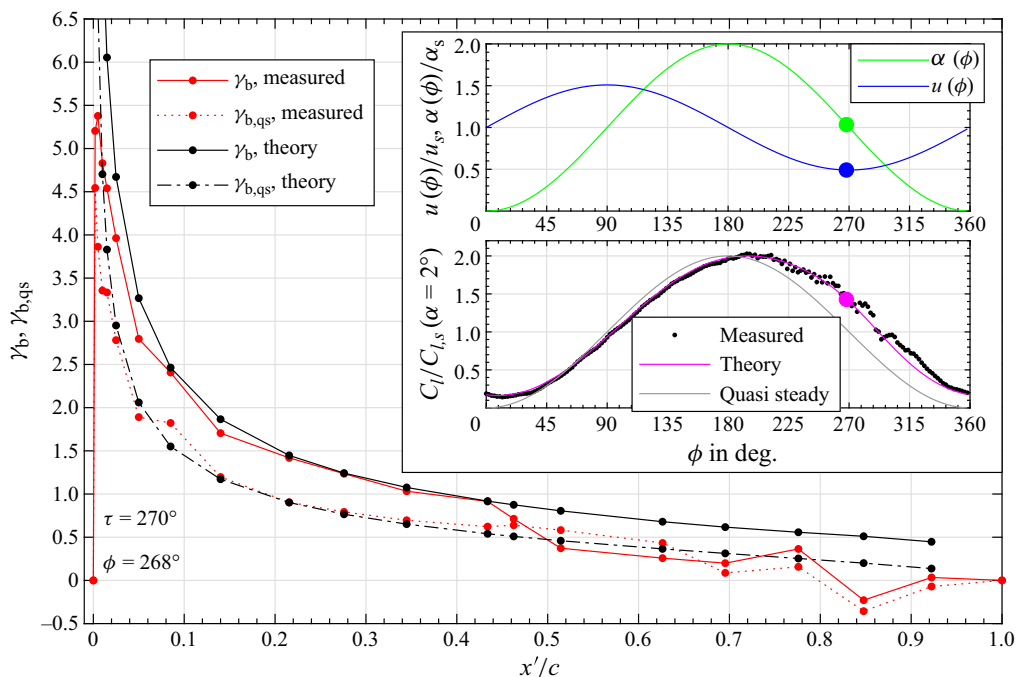
Figure 10. Comparison of measured and theoretical unsteady and quasi-steady bound vortex sheets under synchronous surging and pitching at $\phi = 268°$ and $\tau = 270°$ (see dashed line in figure 9). Insets: free-stream velocity, angle-of-attack and lift coefficient ratios as a function of phase angle.

the normal velocity is negated. In the unsteady case, there are additional normal velocities at the trailing edge and thus the bound vortex sheet must compensate for this. Although this figure presents a compact global comparison between theory and experiment, the reasons for the local deviations from theory are not apparent. To understand the source of the differences, we turn our attention to a representative sample result at the phase lead $\tau = 270°$ for the phase angle $\phi = 268°$, shown in figure 10. This corresponds to the phase angle indicated by the dashed lines on the lowest images in figure 9. The figure contains both unsteady and quasi-steady theoretical and experimental results with insets of α and u (upper inset) and $C_l/C_{l,qs}(\alpha = 2°)$ (lower inset) as functions of ϕ. This comparison is representative of other phase leads as well because significant differences are observed between unsteady and quasi-steady lift coefficients and the separation bubbles are on the verge of bursting (see indicated points in the insets). Over the airfoil surface defined by $0.05 \leqslant \hat{x} \leqslant 0.43$, theoretical unsteady and quasi-steady sheet strengths are very well represented in the experiments (also see the dashed line in figure 9). As the leading edge is approached, from $\hat{x} = 0.05$, significant deviations are observed. This is because the vortex sheet strengths predicted by a flat plate in potential flow tend to infinity as $\hat{x} \to 0$ (Strangfeld *et al.* 2014); this is a well-known limitation of thin airfoil theory. Nevertheless, apart from the measurements at $\hat{x} < 0.01$, the differences between the experimental and theoretical vortex sheet strengths are comparable. For $\hat{x} > 0.62$ deviations from quasi-steady theory are observed and for and $\hat{x} > 0.43$ deviations from unsteady theory are observed. The quasi-steady deviations are due to bubble formation as a result of the adverse spatial pressure gradients, which is well documented (Yarusevych & Kotsonis 2017, and others). The adverse temporal pressure gradient in the unsteady case moves bubble transition upstream, as observed in pure surging flows by Greenblatt *et al.* (2023)
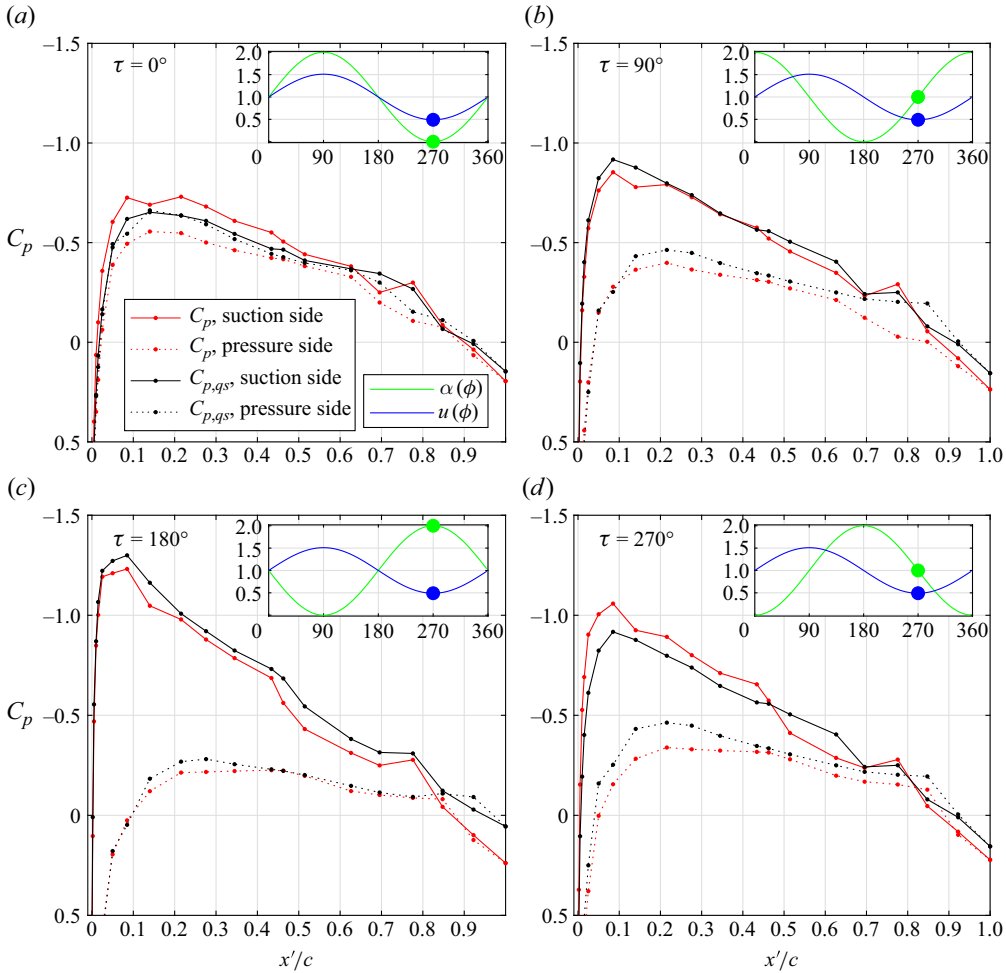
Figure 11. Unsteady and quasi-steady pressure coefficients under synchronous surging and pitching at the end of the deceleration phase ($\phi = 270°$) at four phase differences supplementary movies 3 and 4.

in the angle-of-attack range $0° \leqslant \alpha \leqslant 4°$. Despite the seeming breakdown in theory due to the presence of separation bubbles, correspondence between the theoretical and experimental lift coefficient remains reasonable. Similarly, following bubble bursting at $\phi > 270°$, there are only small deviations from theory, due to the relative importance of the impulsive-pressure lift component discussed in § 4.4.

A limitation of the vortex sheet representation presented here is that it cannot identify the surface on which the separation bubble has formed, because it is based on the pressure differences across the airfoil surface. Consequently, it is also of very little use for examining the mechanisms of bubble bursting. These factors are addressed in the next section which examines the pressure coefficients on the individual surfaces.

4.6. *Bubble-bursting and form drag*

Synchronous unsteady and quasi-steady surface-pressure coefficient distributions at the end of the deceleration phase ($\phi = 270°$) and the early part of the acceleration phase ($\phi = 288°$) are shown in figures 11 and 12, respectively, for the four phase differences τ
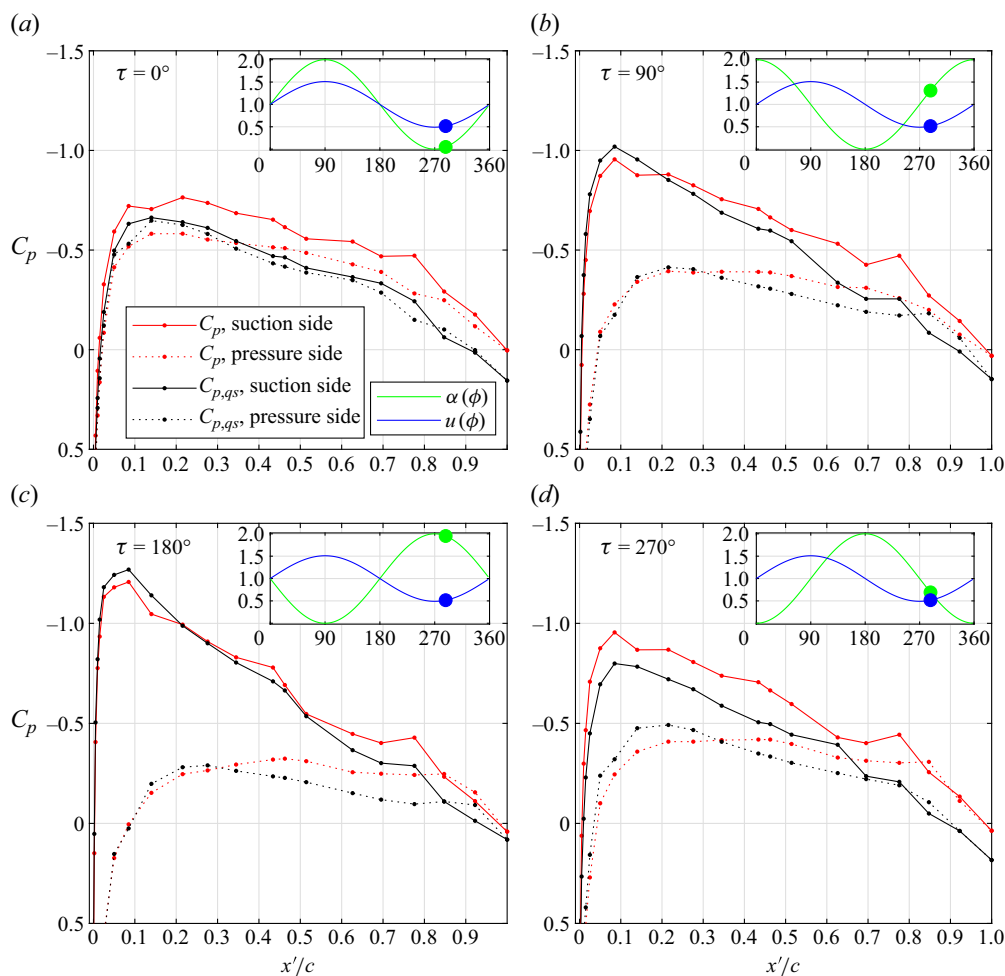
Figure 12. Unsteady and quasi-steady pressure coefficients under synchronous surging and pitching during the early stages of the acceleration phase ($\phi = 288°$) at four phase differences supplementary movies 3 and 4.

supplementary movies 3 and 4. Due to a lack of theory for separation bubbles under surging, a comparison between unsteady and quasi-steady data sets is the only viable method presently to isolate unsteady effects by eliminating Reynolds number as a parameter. From figure 11 (end of the acceleration phase), at $\tau = 0°$, the quasi-steady and unsteady C_p distributions are qualitatively similar, apart from small differences in the region downstream of the leading edge on both surfaces and a local pressure rise on the upper surface at $\hat{x} \approx 0.7$. The latter indicates a possible unsteady effect on transition within the separation bubble. At $\tau = 90°$ and $180°$, the main differences are on the lower surface, where the initiation of the unsteady local pressure recovery occurs upstream of its quasi-steady counterpart. In contrast, at $\tau = 270°$, the start of the upper surface unsteady pressure recovery is upstream relative to the quasi-steady one. Therefore, irrespective of the phase difference, the above observations indicate that the temporal deceleration associated with surging moves transition upstream on either or both of the surfaces, with an overall greater pressure recovery evident at the trailing edge. This also corresponds to upstream movement of the separation point, discussed below.
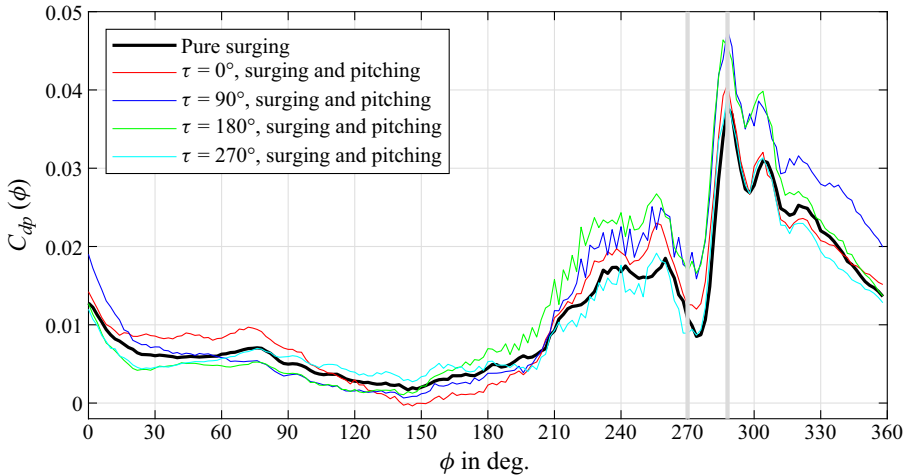
1009 A41-24

Figure 13. Form drag as a function of phase angle under pure surging and synchronous surging and pitching at four phase differences. Conditions corresponding to $\{\sigma, k\} = \{0.51, 0.097\}$ in figure 6. Vertical grey lines correspond to $\phi = 270°$ and $288°$ (see figures 11 and 12).

During the early part of the acceleration phase (see figure 12), the unsteady pressure distributions at all phase differences show a significant pressure drop over the aft part of the airfoil, when compared with the steady data. These pressure drops are a clear manifestation of bubble bursting, irrespective of the corresponding angle-of-attack. It is likely that the lower surface bubble bursts prior to the upper pressure bubble because transition is seen mainly further downstream. Despite the apparent differences in the pressure distributions at different phase differences, the order and mechanism of bubble bursting is essentially the same and occurs at the same phase angles. This assertion is based on measurements of form-drag variation over the cycle, shown together with the pure surging case at $\alpha = 2°$, in figure 13, where $\phi = 270°$ and $288°$ are indicated by vertical grey lines. It can clearly be seen that the phases of the local peaks and troughs correspond precisely for all values of τ and well as for pure surging.

The precise phase correspondence between the pure surging flow and synchronous pitching and surging at all phase differences (figure 13), suggests that the momentum integral analysis used to determine the movement of the separation point in the former (Greenblatt *et al.* 2023) is appropriate here as well. It is based on the well-known Pohlhausen velocity profile (Schlichting & Gersten 2017), together with the generalised boundary layer parameter (Docken Jr 1982)

$$K \equiv \frac{\theta^2}{\nu} \left(\frac{\partial u_e}{\partial s} + \frac{1}{u_e} \frac{\partial u_e}{\partial t} \right), \tag{4.3}$$

where θ is the momentum thickness, u_e is the local velocity on the surface s (assumed to be at the edge of the boundary layer) measured from the stagnation point and $K = -0.1567$ indicates the separation point. For surging and pitching, the unsteady term on the right-hand side of (4.3) can be written as

$$\frac{1}{u_e} \frac{\partial u_e}{\partial t} = \frac{1}{u} \frac{\partial u}{\partial t} - \frac{1}{2(1 - C_p)} \frac{\partial C_p}{\partial t}, \tag{4.4}$$

where the first term is due to surging and does not depend on s, while the second term is mainly due to pitching and depends on both s and t. For the angle-of-attack range
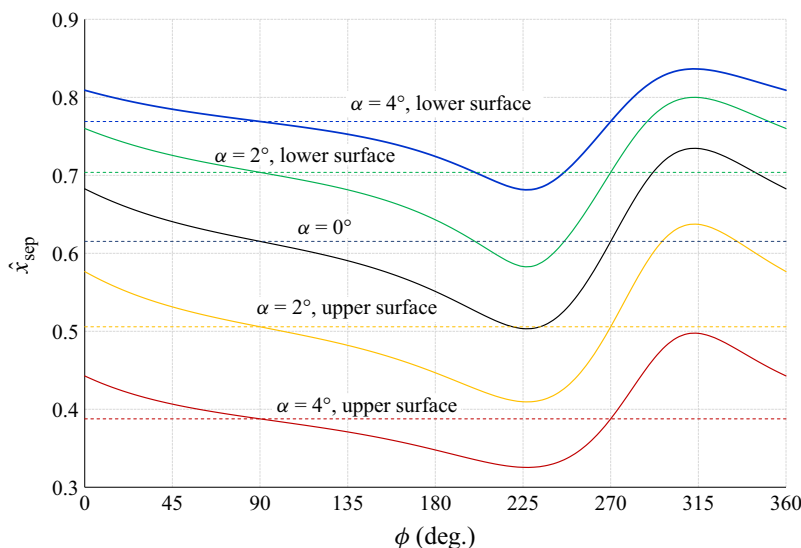
Figure 14. Dimensionless chordwise separation point as a function of phase angle based on quasi-steady boundary layer assumptions; solid lines: quasi-steady momentum integral equation; dashed lines: quasi-steady flow.

considered in this study, the surging term is an order of magnitude greater than the pitching term near the leading edge, and increases to more than two orders of magnitude further along the chord. We can therefore neglect the pitching term and compute the time-dependent separation point, using a vortex lattice method (Drela 1989) to obtain both terms in (4.3). (Strictly speaking, an unsteady vortex lattice method, e.g. Murua, Palacios & Graham (2012) should be used, but for $k \sim 0.1$, the differences are negligible.) The separation point, as a function of the phase angle, is therefore the same as that obtained at constant angles-of-attack and is shown in figure 14 (see Greenblatt *et al.* 2023). It is seen from the figure that deceleration and acceleration phases produce non-symmetric upstream and downstream movements of the separation point, respectively. From $\phi \approx 230°$, the predicted separation point begins to move rapidly downstream, crossing its steady value at $\phi = 270°$, and attaining its furthest downstream location at $\phi \approx 315°$. The figure shows furthermore that the predicted lower surface separation points are further downstream than those on the upper surface, and this is consistent with the observation that bubble transition occurs further downstream on the lower surface in figure 12.

It can be concluded therefore that the unsteady effects on LSB separation and transition are driven predominantly by the surge-induced pressure gradient. However, in order to fully validate these observations, clarifying non-intrusive flowfield measurements, such as particle image velocimetry, must be performed. In future experiments, the bubble bursting can potentially be modified, or eliminated, by tripping both the upper and lower surface boundary layers using, for example, surface roughness strips or 'zig-zag' tape (see Laufer, Frankel & Greenblatt 2022). In the interest of estimating aerodynamic loads at higher Reynolds numbers, boundary layer tripping should be implemented in future research. A limitation of this research was that the angle-of-attack range examined, i.e. $2 \pm 2°$, was relatively small. In future research, larger pre-stall, positive and negative, angle-of-attack ranges should be considered in order to examine the validity of the conclusions drawn here. Furthermore, a larger global reduced frequency range should also be examined. We can estimate this range in the following manner. For the upper limit, we again use $r/c = 7.5$

(Conlisk 2001) as a minimum value, and assume that high-speed rotorcraft advance ratios $\mu > 0.3$. This results in an upper limit $k_{max} = 0.22$, which is conveniently lower than the reduced cutoff frequency of our wind tunnel (see Greenblatt 2016). For the lower limit, we take $\mu = 1$ and $r/c = R/c = 20$, which results in $k_{min} = 0.02$. Examination of (4.1) shows that large regions of so-called 'reverse flow,' i.e. flow from the geometric trailing edge to the geometric leading edge and corresponding to $\sigma > 1$, exist at high advance ratios, inboard of the blade tips. The only facilities that can experimentally replicate these conditions are water-filled towing channels and water tunnels, although generally at much reduced Reynolds numbers (Granlund, Ol & Jones 2016; Kirk & Jones 2019). At present, it appears that only highly resolved computational schemes are capable of reproducing reverse-flow conditions at flight-scaled Reynolds and Mach numbers.

5. Conclusions

This paper presented a combined theoretical and experimental study of synchronous pitching and surging on an airfoil at low pre-stall angles-of-attack ($0° \leqslant \alpha \leqslant 4°$). The theoretical approach was based on the most general formulation of the problem, presented by van der Wall & Leishman (1994), for synchronous pitching and surging at four phase differences, namely $0°$, $90°$, $180°$ and $270°$. The theory was then extended to explicitly compute the unsteady bound vortex sheet strength, which facilitated computation of the individual Joukowsky and impulsive-pressure lift components. Experiments were performed by measuring unsteady surface pressures on a NACA 0018 airfoil, in an unsteady wind tunnel at an average Reynolds number of 3.0×10^5. The majority of unsteady pressure data were acquired at free-stream oscillation amplitudes of 51 %, with an angle-of-attack range of $2° \pm 2°$, and a reduced frequency of 0.097. Quasi-steady surface-pressure data were generated by pitching the airfoil at reduced frequencies of 0.0005, at eleven nominally constant free-stream velocities encompassing the unsteady range and then interpolating pressures at corresponding phases within the unsteady cycle.

Excellent correspondence was obtained between theoretical and experimental lift coefficients for pure pitching throughout the oscillation cycle. Good qualitative correspondence was obtained between pure surging theory and experiments, apart from high-frequency oscillations observed in the experiments during the early stages of the acceleration phase. These oscillations, documented previously by our group, were attributed to bursting of lower and upper surface separation bubbles, which modify the Kutta condition. With synchronous in-phase surging and pitching, excellent correspondence was obtained, representing the first direct experimental validation of the general theory of van der Wall & Leishman (1994). It was shown, both theoretically and experimentally, that the lift coefficient cannot be accurately represented by merely superimposing surging and pitching effects. This is because the effective reduced frequency changes as the free-stream velocity changes, which is not accounted for when pure pitching and pure surging are superimposed. At phase differences of $90°$ and $180°$, large deviations from theory were observed during the beginning of the acceleration phase, and these were attributed to the relative impulsive-lift and Joukowsky contributions to the overall lift coefficient. Specifically, at phase differences of $90°$ and $180°$, the impulsive-lift contributions are small and hence the effect of bubble bursting, which modifies the Kutta condition, has a dominant effect on the overall lift coefficient. The opposite is true for phase differences of $0°$ and $270°$

The correspondence between unsteady theoretical and experimental bound vortex sheet strengths was excellent on the upstream half of the airfoil chord. However, the presence of separation bubbles resulted in a breakdown of this correspondence. Nevertheless, at phase

angles where the impulsive-pressure lift component was dominant, i.e. at phase differences of $0°$ and $270°$, the overall lift coefficient correspondence was strong.

Finally, examination of the airfoil pressure distributions indicated upstream movement of bubble transition on both surfaces, consistent with observations under pure surging. During the early part of the acceleration phase, bubble bursting was identified irrespective of the phase difference. This was consistent with a boundary layer integral analysis that predicted rapid downstream movement of the lower and upper surface separation points. The bursting produced large form-drag oscillations that occurred at identical phase angles within the oscillation cycle, irrespective of the phase difference between surging and pitching, and fully consistent with observations under pure surging. The bubble-bursting dynamic stall mechanism, observed here at low pre-stall angles-of-attack, may have important implications for rotorcraft blade performance and noise emissions.

Appendix A: Experimental Uncertainties

A.1. *Pressure coefficients*

High-precision quasi-steady and unsteady pressure coefficient measurements were performed in order to confidently identify differences between quasi-steady and unsteady effects, while simultaneously accounting for Reynolds number effects. For both quasi-steady and unsteady measurements, the same 99.7 % confidence interval was enforced for all surface-pressure and hot-wire anemometer data.

Quasi-steady surface-pressure coefficients were obtained by recording pressure and hot-wire data at $k = 0.0005$ for 11 nominally constant wind tunnel speeds, in the range $(1 - \sigma)u_s$ to $(1 + \sigma)u_s$. The average surface-pressure coefficients at each even phase angle ϕ_j ($j = 1, \ldots, 180$) was based on the average in the phase window defined by $\phi_j \pm 1°$, resulting in a data points every $2°$, with no overlap between adjacent points. This resulted in $N = 1328$ points per phase window and the maximum pressure coefficient uncertainty recorded for all experiments was $\Delta C_p = \pm 0.0006$, based on a 99.7 % (three standard deviations) confidence interval. At each phase within the oscillation cycle, the pressure coefficients recorded at the nominally constant flow speeds were linearly interpolated to corresponding unsteady $u(\phi_j)$, described below. This provided a quasi-steady surging-and-pitching reference for the unsteady measurements, while simultaneously accounting for Reynolds number effects. More details of this procedure are presented in Müller-Vahl *et al.* (2020).

For unsteady surging and surging-and-pitching experiments, all pressure and hot-wire data within an oscillation cycle were again phase-window averaged $\phi_j \pm 1°$. This procedure resulted in 2 and 3 data points per $2°$ phase window. (This can be seen by the calculation: $f_{daq}/180f$.) In order to obtain at least the same number of points per phase window for both quasi-steady and unsteady data, a total of $N = 1328$ cycles were performed for each experiment (i.e. approximately 20 minutes per experiment). For the same confidence interval as the quasi-steady-flow data (99.7 %), the maximum uncertainty for all experiments, namely $\Delta C_p = \pm 0.0047$, was recorded at the trailing edge at $\tau = 0°$
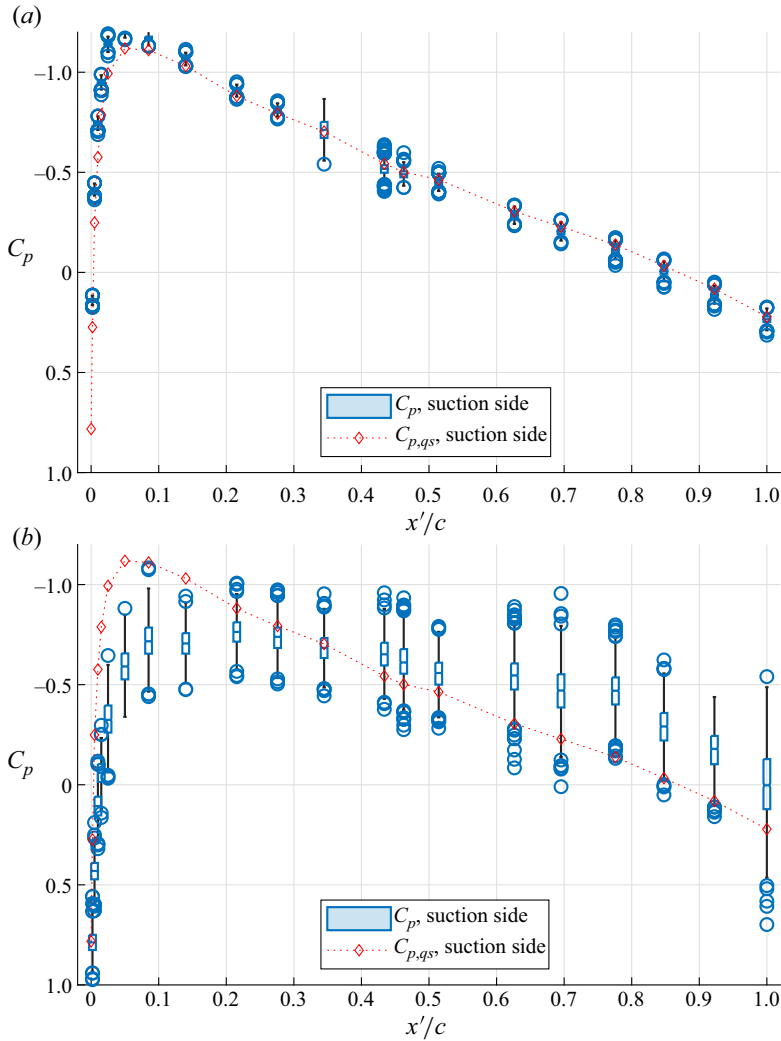
Figure 15. Upper surface pressure coefficient box-and-whisker plots for $\tau = 0°$ corresponding to $\phi = 88°$ (*a*) and $\phi = 288°$ (*b*).

and the phase angle $\phi = 288°$. This phase angle also corresponds to the peak form-drag coefficient, assumed to be associated with bubble bursting, shown in figure 13. Note that, for the steady and unsteady pressure coefficient data shown in figures 11 and 12, even the largest uncertainties are smaller than the circular data symbols and therefore too small to be visualised.

While the phase-averaged pressure coefficient values are of most interest to us, it is well known that separated flows are associated with greater statistical scatter. To visualise this, consider the box-and-whisker plots (DuToit, Steyn & Stumpf 2012) shown in figure 15 for two $\tau = 0°$ phase angles, namely at $\phi = 88°$ and at $\phi = 288°$. In the former case, the flow is attached and only unsteady inviscid effects are present, while the latter case corresponds to the largest recorded uncertainty (at the trailing edge). The median values are shown between 'boxes' that represent the upper and lower quartiles, i.e. 50 % of the total points are contained within the inter-quartile (both boxes) range IQR. The circles represent
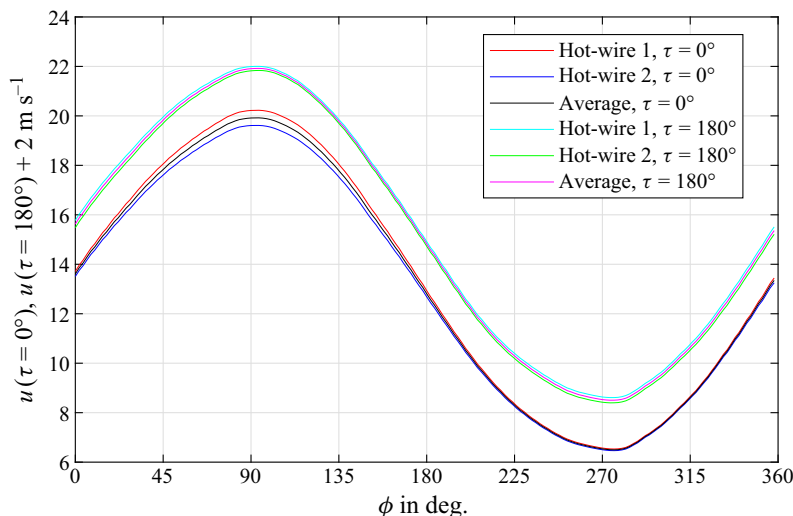
Figure 16. Hot-wire anemometer measurements upstream of the airfoil, above and below, corresponding to synchronous surging and pitching at $\tau = 0°$ and $\tau = 180°$.

'outliers' that are greater than $1.5 IQR$, 'whiskers' (vertical lines) connect the upper or lower quartiles to the non-outlier maxima and minima, respectively, and the 'notches' are $\pm 1.57 IQR/\sqrt{N}$ from the median value. The steady free-stream median values are show as a reference. The boxes show that the data distributions are mainly symmetrical and, much like the uncertainty values given above, the notches on the blocks are impossible to visually discern for $\phi = 88°$ and difficult to visualise for $\phi = 288°$ due to the larger number of data points (N) recorded. On the other hand, the outliers give an indication of the scatter associated with the data. They are, in fact, valid data points and therefore not excluded from the data sets and are shown here to provide an indication of the data scatter. For the $\phi = 88°$ case, relatively large scatter is associated with the bubble separation and reattachment, while for the $\phi = 288°$ case, there is particularly large scatter associated with all data points. This is because, even though the the bubble-bursting effects are most pronounced at the trailing edge, bursting affects the instantaneous circulation and hence the surface pressure at all points on the airfoil.

A.2. *Velocity and turbulence measurements*

For all experiments, the velocity measurements of hot-wires 1 and 2, above and below the airfoil (see figure 2), were averaged. Repeated calibrations produced velocity variations between the two wires of no more than 0.25 %, but during surging, a consistent 1 % difference between the wires was observed. It was also discovered that the difference between the wires increased with angle-of-attack for both steady and unsteady experiments. To illustrate these observations, consider in-phase ($\tau = 0°$) and anti-phase ($\tau = 180°$) surging-and-pitching results, with the latter shifted by 2 m s^{-1} for clarity, in figure 16. The results for both wires, as well as their averages, are shown. For the in-phase case, the maximum relative differences between the upper and lower measurements are 3 % and 1 %, at $\phi = 90°$ and $270°$, respectively. The opposite is true, namely 1 % and 3 % differences, at $\phi = 90°$ and $270°$, respectively, for the anti-phase case. The larger differences (i.e. 3 %) occur at the maximum angle-of-attack, irrespective of surging, because the lower pressure on the upper surface of the airfoil increases the local mass flowrate above the airfoil. For the test-section mass to be conserved, the flowrate below

1009 A41-30

the airfoil must be lower by a proportional amount. Averaging the two therefore produces a representative estimate of the average tunnel velocity. Gradients such as these are an unavoidable artefact of two-dimensional airfoil experiments of the type described here, and in many similar experiments reported on in the literature, these gradients are simply neglected.

The effect of the louvers on the wind tunnel turbulence was investigated by Greenblatt (2016) and a summary is presented here. At a wind tunnel speed of 13.9 m s^{-1}, it was determined that the nominal turbulence level without louvers present was $Tu \equiv u'/u_s < 0.1$ %, where u' is the root-mean-square of the free-stream oscillations. The value of Tu increased to values greater than 0.1 % when the louvers were installed and partially closed. However, frequency spectra revealed that the vortex shedding from the louver blades excited the Helmholtz frequency of the tunnel, $f_H \approx 7$ Hz, with insignificant changes to the other frequencies, and high-pass filtering at 20 Hz resulted in $Tu < 0.1$ %. It was concluded that this low frequency had very little effect on the bubble because the convective inflectional instability frequencies and the lower bubble shedding frequencies are both much higher than the tunnel Helmholtz frequency. Numerically, the lowest bubble shedding frequency encountered during the cycle is $f_{sh} > 0.5u_s(1 - \sigma)/L_b = \mathcal{O}(10^2)$. Assuming a bubble length $L_b = 0.1c$, the bubble shedding frequency is $f_{sh} \approx 95$ Hz, which is an order of magnitude greater than the Helmholtz frequency. It was thus concluded that the tunnel Helmholtz frequency had no meaningful effect on the airfoil separation bubbles.

REFERENCES

AMIET, R.K. 1990 Gust response for flat-plate airfoils and the Kutta condition. *AIAA J.* **28** (10), 1718–1727.

ANDERSON, J.D. 2011 *Fundamentals of Aerodynamics*. McGraw-Hill Education.

BARBELY, N.L. & KOMERATH, N.M. 2016 Coaxial rotor flow phenomena in forward flight. In *2016 International Powered Lift Conference (IPLC)/SAE Aerospace Systems and Technology Conference*

BERGAMI, L., GAUNAA, M. & HEINZ, J. 2013 Indicial lift response function: an empirical relation for finite-thickness airfoils, and effects on aeroelastic simulations. *Wind Energy* **16** (5), 681–693.

BISPLINGHOFF, R.L., ASHLEY, H. & HALFMAN, R.L. 2013 *Aeroelasticity*. Courier Corporation.

BUCHNER, A.-J., SORIA, J., HONNERY, D. & SMITS, A.J. 2018 Dynamic stall in vertical axis wind turbines: scaling and topological considerations. *J. Fluid Mech.* **841**, 746–766.

CARMICHAEL, B.H. 1981 Low Reynolds number airfoil survey, volume 1. *Tech. Rep.* NASA-CR-165803-VOL-1. Low Energy Transportation Systrems, Capistrano Beach, California (United States). https://ntrs.nasa.gov/citations/19820006186

CHOI, J., COLONIUS, T. & WILLIAMS, D.R. 2015 Surging and plunging oscillations of an airfoil at low Reynolds number. *J. Fluid Mech.* **763**, 237–253.

CONLISK, A.T. 2001 Modern helicopter rotor aerodynamics. *Prog. Aerosp. Sci.* **37** (5), 419–476.

CORKE, T.C. & THOMAS, F.O. 2015 Dynamic stall in pitching airfoils: aerodynamic damping and compressibility effects. *Annu. Rev. Fluid Mech.* **47** (1), 479–505.

DOCKEN, JR & RICHARD, G. 1982 Gust response prediction of an airfoil using a modified von Karman-Pohlhausen technique, Master's thesis. Air Force Institute of Technology, Air University, Ohio, USA.

DRELA, MARK 1989 XFOIL: An analysis and design system for low Reynolds number airfoils. In *Low Reynolds Number Aerodynamics*, pp. 1–12. Springer.

DUNCAN, LUCAS, CAI, JIELONG & GUNASEKARAN, SIDAARD 2024 Powered wing's response to streamwise gust encounters. In *AIAA SCITECH. 2024 Forum*, pp. 0077.

DUNNE, R. & MCKEON, B.J. 2015 Dynamic stall on a pitching and surging airfoil. *Exp. Fluids* **56** (8), 1–15.

DUTOIT, S.H.C., STEYN, A.G.W. & STUMPF, R.H. 2012 *Graphical Exploratory Data Analysis*. Springer Science & Business Media.

FEIL, R., HAJEK, M. & RAULEDER, J. 2020 Vibratory load predictions of a high-advance-ratio coaxial rotor system validated by wind tunnel tests. *J. Fluids Struct.* **92**, 102764.

FERREIRA, C.S., KUIK, G.V., BUSSEL, G.V. & SCARANO, F. 2009 Visualization by PIV of dynamic stall on a vertical axis wind turbine. *Exp. Fluids* **46** (1), 97–108.

GARDNER, A.D., JONES, A.R., MULLENERS, K., NAUGHTON, J.W. & SMITH, M.J. 2023 Review of rotating wing dynamic stall: experiments and flow control. *Prog. Aerosp. Sci.* **137**, 100887.

GASTER, M. 1967 *The structure and behaviour of laminar separation bubbles*. Citeseer.

GLOUTAK, D., JANSEN, K.E. & FARNSWORTH, J.A. 2024 Aerodynamic performance of a finite-span wing in a time-varying freestream. *AIAA J.* **62** (6), 2248–2263.

GRANLUND, K., MONNIER, B., OL, M. & WILLIAMS, D. 2014 Airfoil longitudinal gust response in separated vs. attached flows. *Phys. Fluids* **26** (2), 1–14.

GRANLUND, K.O., OL, M.V. & JONES, A.R. 2016 Streamwise oscillation of airfoils into reverse flow. *AIAA J.* **54** (5), 1628–1636.

GREENBERG, J.M. 1947 Airfoil in sinusoidal motion in a pulsating stream. *NACA Technical Note* No. 1326, Washington, June.

GREENBLATT, D. 2016 Unsteady low-speed wind tunnels. *AIAA J.* **54** (6), 1817–1830.

GREENBLATT, D., KIEDAISCH, J. & NAGIB, H. 2001 Unsteady-pressure corrections in highly attenuated measurements at moderate Mach numbers. In *15th AIAA Computational Fluid Dynamics Conference*. 11 June 2001 - 14 June 2001 Anaheim, CA, U.S.A. https://doi.org/10.2514/6.2001-2983. pp. 2983

GREENBLATT, D., MÜLLER-VAHL, H. & STRANGFELD, C. 2023 Laminar separation bubble bursting in a surging stream. *Phys. Rev. Fluids* **8** (1), L012102.

ISAACS, R. 1945 Airfoil theory for flows of variable velocity. *J. Aeronaut. Sci.* **12** (1), 113–117.

ISAACS, R. 1946 Airfoil theory for rotary wing aircraft. *J. Aeronaut. Sci.* **13** (4), 218–220.

JONES, A.R., CETINER, O. & SMITH, M.J. 2022 Physics and modeling of large flow disturbances: discrete gust encounters for modern air vehicles. *Annu. Rev. Fluid Mech.* **54** (1), 469–493.

KIRK, P.B. & JONES, A.R. 2019 Vortex formation on surging aerofoils with application to reverse flow modelling. *J. Fluid Mech.* **859**, 59–88.

LAUFER, M., FRANKEL, S.H. & GREENBLATT, D. 2022 GPU-accelerated implicit large eddy simulation of a NACA, 0018 airfoil with active flow control. In *AIAA SCITECH. 2022 Forum*, pp. 0471.

LEE, S., AYTON, L., BERTAGNOLIO, F., MOREAU, S., CHONG, T.P. & JOSEPH, P. 2021 Turbulent boundary layer trailing-edge noise: theory, computation, experiment, and application. *Prog. Aerosp. Sci.* **126**, 100737.

LIND, A.H., SMITH, L.R., MILLUZZO, J.I. & JONES, A.R. 2016 Reynolds number effects on rotor blade sections in reverse flow. *J. Aircraft* **53** (5), 1248–1260.

MA, R., YANG, Y., LI, M. & LI, Q. 2021 The unsteady lift of an oscillating airfoil encountering a sinusoidal streamwise gust. *J. Fluid Mech.* **908**, A22.

MARXEN, O. & HENNINGSON, D.S. 2011 The effect of small-amplitude convective disturbances on the size and bursting of a laminar separation bubble. *J. Fluid Mech.* **671**, 1–33.

MEDINA, A., OL, M.V., GREENBLATT, D., MÜLLER-VAHL, H. & STRANGFELD, C. 2018 High-amplitude surge of a pitching airfoil: complementary wind- and water-tunnel measurements. *AIAA J.* **56** (4), 1703–1709.

MOTTA, V., GUARDONE, A. & QUARANTA, G. 2015 Influence of airfoil thickness on unsteady aerodynamic loads on pitching airfoils. *J. Fluid Mech.* **774**, 460–487.

MÜLLER-VAHL, H.F., PECHLIVANOGLOU, G., NAYERI, C.N., PASCHEREIT, C.O. & GREENBLATT, D. 2017 Matched pitch rate extensions to dynamic stall on rotor blades. *Renew. Energy* **105**, 505–519.

MÜLLER-VAHL, H.F., STRANGFELD, C., NAYERI, C.N., PASCHEREIT, C.O. & GREENBLATT, D. 2020 Dynamic stall under combined pitching and surging. *Am. Inst. Aeronaut. Astronaut. J.* **58** (12), 5134–5145.

MURUA, J., PALACIOS, R. & GRAHAM, J.M.R. 2012 Applications of the unsteady vortex-lattice method in aircraft aeroelasticity and flight dynamics. *Prog. Aerosp. Sci.* **55**, 46–72.

NAGIB, H., KIEDAISCH, J., GREENBLATT, D., WYGNANSKI, I. & HASSAN, A. 2001 Effective flow control for rotorcraft applications at flight Mach numbers. In *15th AIAA Computational Fluid Dynamics Conference*, pp. 2974. 11 June 2001 - 14 June 2001. Anaheim,CA,U.S.A. https://doi.org/10.2514/6.2001-2974

OO, N.L., ZHAO, D., SELLIER, M. & LIU, X. 2023 Experimental investigation on turbulence effects on unsteady aerodynamics performances of two horizontally placed small-size UAV rotors. *Aerosp. Sci. Technol.* **141**, 108535.

SCHADE, H., KUNZ, E., KAMEIER, F. & PASCHEREIT, C.O. 2007 *Strömungslehre*, 3rd edn. Walter de Gruyter.

SCHLICHTING, H. & GERSTEN, K. 2017 *Boundary Layer Theory*. 9th edition, vol. 121. Springer.

SHARMA, A. & VISBAL, M. 2019 Numerical investigation of the effect of airfoil thickness on onset of dynamic stall. *J. Fluid Mech.* **870**, 870–900.

SIMMS, D., SCHRECK, S., HAND, M. & FINGERSH, L.J. 2001 NREL unsteady aerodynamics experiment in the NASA-Ames wind tunnel: a comparison of predictions to measurements. *Tech. Rep.* NREL/TP-500-29494. National Renewable Energy Lab, Golden, Colorado (United States). https://doi.org/10.2172/783409

SINGH, P. & FRIEDMANN, P.P. 2021 Aeromechanics and aeroelastic stability of coaxial rotors. *J. Aircraft* **58** (6), 1386–1405.

STRANGFELD, CHRISTOPH 2015 Active control of trailing vortices by means of long- and short-wavelength actuation *PhD thesis*. Technische Universität, Berlin.

STRANGFELD, C., MUELLER-VAHL, H., GREENBLATT, D., NAYERI, C. & PASCHEREIT, C.O. 2014 Airfoil subjected to high-amplitude free-stream oscillations: theory and experiments. In *7th AIAA Theoretical Fluid Mechanics Conference* 16-20 June. Atlanta, GA. https://doi.org/10.2514/6.2014-2926

STRANGFELD, C., MÜLLER-VAHL, H., NAYERI, C.N., PASCHEREIT, C.O. & GREENBLATT, D. 2016 Airfoil in a high amplitude oscillating stream. *J. Fluid Mech.* **793**, 79–108.

TAHA, H. & REZAEI, A.S. 2019 Viscous extension of potential-flow unsteady aerodynamics: the lift frequency response problem. *J. Fluid Mech.* **868**, 141–175.

TAYLOR, G.K., NUDDS, R.L. & THOMAS, A.L.R. 2003 Flying and swimming animals cruise at a Strouhal number tuned for high power efficiency. *Nature* **425** (6959), 707–711.

THEODORSEN, T. 1935 General theory of aerodynamic instability and the mechanism of flutter. *NACA Rep.* No. 496 pp. 291–311.

TOPPINGS, C. & YARUSEVYCH, S. 2023 Transient dynamics of laminar separation bubble formation and bursting. *Exp. Fluids* **64** (57), 1–15.

TURHAN, B., WANG, Z. & GURSUL, I. 2022 Coherence of unsteady wake of periodically plunging airfoil. *J. Fluid Mech.* **938**, A14.

VAN DER WALL, B.G. 1991 The influence of variable flow velocity on unsteady airfoil behavior. Master of Science Thesis, University of Maryland.

VAN DER WALL, B.G. & LEISHMAN, J.G. 1994 On the influence of time-varying flow velocity on unsteady aerodynamics. *J. Am. Helicopter Soc.* **39** (4), 25–36.

WANG, T., FENG, L.-H., CAO, Y.-T. & WANG, J.-J. 2024 Airfoil response to periodic vertical and longitudinal gusts. *J. Fluid Mech.* **979**, A35.

YANG, Y., LI, M., MA, C. & LI, S. 2017 Experimental investigation on the unsteady lift of an airfoil in a sinusoidal streamwise gust. *Phys. Fluids* **29** (5), 051703-1–051703-6.

YARUSEVYCH, S. & KOTSONIS, M. 2017 Steady and transient response of a laminar separation bubble to controlled disturbances. *J. Fluid Mech.* **813**, 955–990.

ZHU, W., MCCRINK, M.H., BONS, J.P. & GREGORY, J.W. 2020 The unsteady Kutta condition on an airfoil in a surging flow. *J. Fluid Mech.* **893**, R2-1–R2-12.